Geophysical Journal International

Geophys. J. Int. (2019) **219,** 313–327 doi: 10.1093/gji/ggz298
Advance Access publication 2019 July 02
GJI Seismology

Constraining crustal structure in the presence of sediment: a multiple converted wave approach

Erin Cunningham and Vedran Lekic

Department of Geology, University of Maryland, College Park, MD 20742, *USA. E-mail:* ecunnin2@umd.edu

Accepted 2019 June 28. Received 2019 June 19; in original form 2018 July 12

SUMMARY

Receiver functions are sensitive to sharp seismic velocity variations with depth and are commonly used to constrain crustal thickness. The *H*–*κ* stacking method of Zhu & Kanamori is often used to constrain both the crustal thickness (*H*) and V_P/V_S ratio (*κ*) beneath a seismic station using P-to-s converted waves (Ps). However, traditional *H*–*κ* stacks require an assumption of average crustal velocity (usually V_P). Additionally, large amplitude reverberations from low velocity shallow layers, such as sedimentary basins, can overprint sought-after crustal signals, rendering traditional *H*– *κ* stacking uninterpretable. We overcome these difficulties in two ways. When *S*-wave reverberations from sediment are present, they are removed by applying a resonance removal filter allowing crustal signals to be clarified and interpreted. We also combine complementary Ps receiver functions, Sp receiver functions, and the post-critical *P*-wave reflection from the Moho (SP_mp) to remove the dependence on an assumed average crustal V_P. By correcting for sediment and combining multiple data sets, the crustal thickness, average crustal *P*-wave velocity and crustal V_P/V_S ratio is constrained in geological regions where traditional *H*– *κ* stacking fails, without making an initial *P*-wave velocity assumption or suffering from contamination by sedimentary reverberations.

Key words: Time-series analysis; Body waves; Crustal imaging; Site effects.

1 INTRODUCTION

Across a sharp seismic impedance contrast, some of the seismic energy from direct teleseismic *P* waves converts to SV wave energy, and vise versa. Receiver functions (RFs) isolate the time series of converted wave energy directly beneath a seismic station by deconvolving the parent waveform (P for P-to-s conversions and S for S-to-p) from the daughter waveform (S for Ps and P for Sp), removing complexity in the signal due to earthquake rupture and distant structure. RFs are sensitive to sharp seismic velocity variations with depth and are therefore used to constrain shallow crustal and lithospheric velocity discontinuities such as the boundary between the crust and mantle (Mohorovičić discontinuity or Moho, e.g. Vinnik 1977; Langston 1979; Owens *et al.* 1984). Stacking the amplitudes of RFs at the expected arrival times of the converted phase across the Moho and its primary reverberations (multiples) for a range of crustal thickness (*H*) and relative velocity (V_P/V_S ratio or *κ*) values will produce a maximum of the stack corresponding to the best estimate for *H* and *κ* (Zhu & Kanamori 2000). Due to its simplicity and exploitation of both direct converted and reverberating phases, *H*–*κ* stacking has become a widely used method to obtain an estimate of the average crustal thickness and velocity beneath a seismic station. Traditional *H*–*κ* stacking has been used extensively to estimate the thickness and V_P/V_S of the crust (Kumar *et al.* 2001a; Ramesh *et al.* 2002; Eaton *et al.* 2006; Rychert *et al.* 2007; Audet *et al.* 2009; French *et al.* 2009; Yuan *et al.* 2010; Levander & Miller 2012; Parker *et al.* 2013; Reeves *et al.* 2015; Biryol *et al.* 2018; Soto-Cordeo *et al.* 2018). With the deployment of large-scale seismic arrays, such as the EarthScope USArray, automated RF analysis in the form of *H*–*κ* stacking has been deployed to constrain crustal structure on a continental scale (Crotwell & Owens 2005). While straightforward, the traditional method of Ps *H*–*κ* stacking is limited by two major factors: (1) the prior assumption of an average crustal velocity beneath a seismic station and (2) contamination of crustal signal by sediment or other shallow-layer reverberations. These limitations have proved difficult to overcome, and can significantly bias estimates of crustal thickness and V_P/V_S ratios based on them.

Several studies have quantified how assuming an incorrect average V_P can bias crustal thickness and V_P/V_S estimates from *H*–*κ* stacks by up to 10 s of kilometres for *H* (Sheehan *et al*. 1995; Zelt & Ellis 1999; Yeck *et al.* 2013). At some locations, an accurate crustal velocity may be obtained from active source experiments or surface wave inversion studies; however, a continental scale study requires that these measurements are available at all locations and reflect the same region of lateral sensitivity as the receiver functions (Chai *et al.* 2015; Rychert & Harmon 2016). Though Ps RFs do have some sensitivity to average crustal V_P (Kumar & Bostock 2008; Bostock & Kumar 2010), it is typically insufficient to provide robust estimates of V_P beneath the seismic station. Therefore, to remove the dependence on V_P, Sp RFs can be combined with Ps RFs to create stacks that constrain average crustal H, V_P and V_S (Rychert & Harmon 2016). The S-to-p wave conversion from the Moho arrives before the direct S, meaning that Sp RFs are not contaminated by sediment reverberations in the same way as Ps RFs (Farra & Vinnik 2000), although, Sp RFs have a smaller amplitude conversions and typically contain energy at lower dominant frequencies than Ps RFs. Because vertical resolution depends on frequency content, lower frequency Sp RFs yield a lesser vertical resolution. Due to the relatively low signal to noise ratio of Sp converted phases, the large amplitude post critical P reflection from the Moho, called the SP_mp phase, can be used to constrain average crustal P-wave velocity (Langston 1996; Owens & Zandt 1997; Yu *et al.* 2012; Kang *et al.* 2016; Parker *et al.* 2016). While the SP_mp phase has a broad region of lateral sensitivity, it is less impacted by sediment reverberations and depends on average crustal V_P and crustal thickness, rather than V_S.

However, even once crustal V_P is well constrained, a slow sedimentary layer beneath a seismic station can significantly bias crustal thickness estimates (Yeck *et al.* 2013) and large amplitude sediment reverberations can directly overprint Ps conversions from the Moho, rendering interpretation of Ps H–κ stacks challenging (Zelt & Ellis 1999). Previous studies have removed sediment reverberations with some success, but these methods fail if more than one sedimentary layer exists or if sedimentary phase arrivals directly overlap Moho arrivals. (Yeck *et al.* 2013; Wölbern & Rümpker 2017), and require an assumption about average crustal V_P (Yu *et al.* 2015). Currently no single method overcomes limitations of traditional H–κ stacking, the assumption of crustal V_P, and contamination by one or many sedimentary layers.

To constrain average crustal thickness, V_P and V_P/V_S in sediment dominated regions, contamination from sediment reverberations should be removed and data with complementary sensitivity should be incorporated. We propose a method that applies a resonance removal filter to Ps RFs when contaminated by sediment, and combines these sediment-removed Ps RFs with Sp RFs as well as the envelopes of SP_mp RFs. Stacking these three complementary datasets across a range of H, κ and V_P and accounting for slowness in sedimentary layers yields a maximum at H, κ and V_P values corresponding to the best estimate of all three crustal parameters. This method is called the sediment-removed, time-corrected (SRTC) H–κ–V_P triple stack. The ability of this method to constrain the crustal structure is demonstrated using synthetic data and results from three different geological/tectonic regions using recordings from USArray Temporary Array (TA) stations. The two main benefits of this method are that it constrains all three crustal parameters in regions where sediment reverberations contaminate Ps RFs and that it can be automated to calculate these values for continental scale seismic arrays such as the EarthScope USArray.

2 METHODS

By removing source and path effects through deconvolution, receiver functions isolate the near receiver structure. Deconvolution can be performed in the frequency domain using modified spectral division (Clayton & Wiggins 1976; Bostock 1996; Dueker & Sheehan 1997; Lawerence & Shearer 2006); however, we choose to use the time domain simultaneous least squares deconvolution of Kikuchi & Kanamori (1982) and Ligorria & Ammon (1999) to reduce the appearance of side lobes. (For a full discussion of receiver function deconvolution techniques see Pesce 2010.) Traditionally,

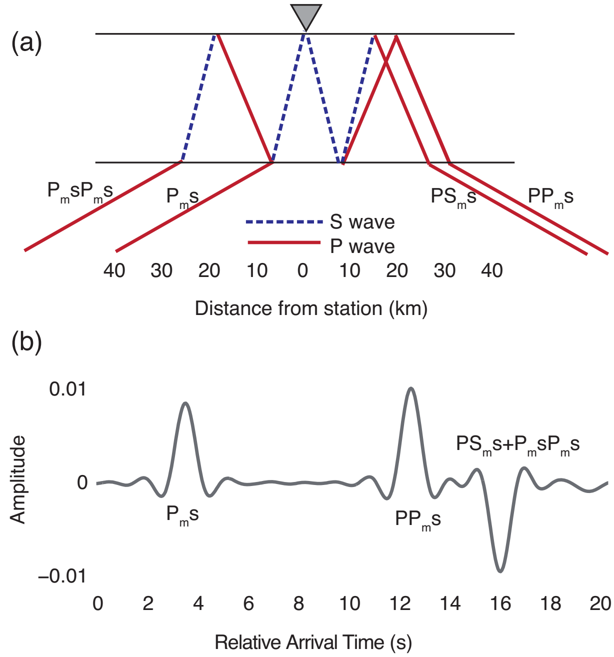

Figure 1. (a) Ray path geometry and (b) synthetic receiver functions of P-to-s phases converted across the Moho at 30 km depth, from an incident plane wave of horizontal slowness 0.06 s km^{-1}. Crustal $V_P = 6.3$ km s^{-1}, $V_S = 3.7$ km s^{-1}, while mantle $V_P = 8$ km s^{-1} and $V_S = 4.6$ km s^{-1}. Arrival times of the direct Moho P-to-s conversion and first-order multiples are relative to the arrival time of the direct P wave.

these Ps RFs are calculated and then stacked along predicted phase arrival times over a range of crustal thickness (H) and crustal velocity (V_P/V_S ratio or κ) to create H–κ stacks (Zhu & Kanamori 2000).

In this study, we review traditional H–κ stacking (Section 2.1) and then introduce the approach for removing and correcting for shallow-layer reverberations (Section 2.2), which is based on the resonance removal filter of Yu *et al.* (2015). We then introduce and discuss metrics that allow us to determine when the shallow-layer corrections are needed (Section 2.3). Once contamination from sediment reverberations has been removed, the complementary Sp (Section 2.4) and SP_mp (Section 2.5) data are added to form a SRTC H–κ–V_P triple stack (Section 2.6). This SRTC H–κ–V_P stack explicitly removes the need to assume a crustal velocity, and thereby improves confidence in our estimates of crustal thickness and velocity.

2.1 Ps receiver functions in traditional H–κ–V_P stacks

The direct P-to-s conversion across the Moho (P_ms) is often used to constrain the Moho depth. The Moho depth estimate can be improved by including the multiple later arriving P-to-s primary reverberations, PP_ms, and $PS_ms + P_msP_ms$ whose ray paths are shown in Fig. 1(a) and relative arrival times are shown in Fig. 1(b). The expected arrival time of the direct conversion and primary reverberations relative to the direct P wave arrival depend differently on crustal thickness (H) and crustal velocity (V_P and V_S) given a ray parameter (p) of the teleseismic P wave:

$$t_{P_ms} = H\left(\sqrt{V_S^{-2} - p^2} - \sqrt{V_P^{-2} - p^2}\right) \quad (1)$$

$$t_{PP_{m}s} = H\left(\sqrt{V_S{}^{-2} - p^2} + \sqrt{V_P{}^{-2} - p^2}\right) \quad (2)$$

$$t_{PS_{m}s} + t_{P_{m}sP_{m}s} = 2H\sqrt{V_S{}^{-2} - p^2} \quad (3)$$

Each Ps receiver function, $f_j(t)$, corresponds to incident *P* waves of ray parameter, p_j, where j is the index of the individual RF. By assuming H, κ and an average crustal velocity, V_P, eqs (1)–(3) are used to compute the expected arrival times of the direct conversions and reverberations. The weighted sum of all *N* Ps receiver functions obtained at a seismometer are evaluated at the arrival times expected across a range of trial *H* and κ values to yield an *H*–κ stack:

$$s_{Ps}\ (H, \kappa) = \sum\nolimits_{j=1}^{N} w_1 f_j\left(t_{P_{m}s}\right) + w_2 f_j\left(t_{PP_{m}s}\right) - w_3 f_j\left(t_{PS_{m}s} + t_{P_{m}sP_{m}s}\right), \quad (4)$$

where w_1, w_2 and w_3 are the relative weights of the three phases. The most likely *H* and κ beneath the seismic station will be associated with largest amplitudes of the weighted sum, s_{Ps} using the same weight values as Zhu & Kanamori (2000) where $w_1 = 0.7$, $w_2 = 0.2$ and $w_3 = 0.1$.

In theory, Ps receiver functions spanning a range of ray parameters should contain information needed to constrain V_P on their own when stacked over a range of *H*, κ and V_P values (Kumar & Bostock 2008; Bostock & Kumar 2010). Therefore Ps RF stacks are calculated over a range of average crustal V_P values creating a Ps RF *H*–κ–V_P triple stack and is called $s_{Ps}(H, \kappa, V_P)$, where the absolute maximum should correspond to the most likely average crustal values beneath the seismic station. In practice, when shallow-layer reverberations are present, it is necessary to first remove their signature before determining V_P; this procedure is discussed in Section 2.2. Furthermore, noise in the receiver functions and the range of incident ray parameters can prevent robust estimation of V_P, requiring the incorporation of independent data constraints; these independent constraints are discussed in Sections 2.3 and 2.4.

2.2 SRTC Ps receiver function H–κ–V_P stacks

When sedimentary layers are present, energy from conversions produced across the impedance contrast at the base of the sediment and reverberations within the sediment can get trapped within the low-velocity layer. These conversions and reverberations can produce large amplitude, long duration and oscillatory (ringy) signals, which can directly overprint smaller amplitude signals from the Moho. The ray paths for the direct sediment conversion P_bs, and reverberations PP_bs, PS_bs, P_bs-2S, PP_bs-2S, PS_bs-2S, P_bs-4S, etc. are shown in Fig. 2(a), and relative arrival times are shown in Fig. 2(b). In Ps receiver functions, the largest amplitude, longest duration oscillatory reverberations are those that contain two S-legs in the sediment (the *S*-wave reverberations: PS_bs, P_bs-2S, PP_bs-2S, P_bs-4S, etc. Fig. 2b). The reverberations at longer times contain primarily *S*-wave energy due to fact that Ps receiver functions are computed from upgoing *P* and *S* waveforms estimated using the free-surface transform (Kennett 1991), and because the $\grave{S}\acute{S}$ reflection coefficient at the base of the layer is large, as shown in Fig. S1. It is important to note that though the PP_bs phase arrival itself has large amplitude, it would only interfere with the P_ms Moho conversion when the crust is extremely thin (<20 km) and the sediment is both thick and unreasonably slow, as shown in Fig. S2 for a range of sediment velocities and thicknesses. Therefore, to interpret later arriving Moho signals in the Ps receiver function, the periodic *S*-wave sediment reverberations must often be removed.

The *S*-wave sediment reverberations can be suppressed from the Ps RF by applying a resonance removal filter proposed by Yu *et al.* (2015). The *S* reverberations have a resonant frequency associated with the two-way traveltime of the *S* wave in the sediment layer. A resonance removal filter can be constructed using the traveltime of the *S* reverberation in sediment, Δt, and the relative strength of the *S*-wave reverberation, r_0 While these values can be inferred directly from the Ps RF, both Δt and r_0 can be more reliably measured on the autocorrelation of the receiver function. In sediment, the autocorrelation of the Ps RF will have a decaying sinusoid pattern, showing a large, negative peak with amplitude r_0, at time lag Δt (Fig. 3a). A consistent method for determining these parameters, even when the autocorrelation is complex and contains multiple minima (which suggests multiple shallow layers), involves finding the best-fitting decaying sinusoid to the autocorrelation function of the form:

$$m(t) = ce^{-at}\cos\left(\frac{\pi t}{\Delta t}\right), \quad (5)$$

where *t* is the lag time of the autocorrelated RF, and the three parameters sought through the fitting procedure are the half-period of the oscillation, Δt, the amplitude of the autocorrelation at zero lag time, c, and the decay constant a. Because the half-period of the oscillation is precisely the traveltime of the *S* reverberation, $m(\Delta t) = r_0$, both parameters of the resonance removal filter can be estimated (Fig. 3a). While these parameters should depend somewhat on ray parameter, the lateral proximity of the *S* reverberation bounce points to the station for the range of teleseismic ray parameters means that this dependence is in practice small enough that computing a single best-fitting set of parameters across all ray parameters is justified (illustrated for the idealized synthetic case in Fig. S3). For example, when sediment is 2-km-thick with a $V_P = 2.5\ \mathrm{km\,s^{-1}}$ and $V_S = 2.1\ \mathrm{km\,s^{-1}}$, the PS_bs reflection for an event with epicentral distance of 90° may occur just 0.19 km from the station, while that for an event with epicentral distance of 30° will occur 0.37 km from the station. Therefore the best-fitting decaying sinusoid is found to the autocorrelation of the mean Ps RF at the station. The benefit to using eq. (5) is that it can be easily automated and may help simplify the interpretations of Δt in complicated or noisy autocorrelated signals. Furthermore, calculating the resonance removal filter on the mean Ps receiver function at each station has the benefit of leveraging more waveforms to suppress noise and thereby stabilizes the inference of the optimal resonance removal filter parameters.

Once the parameters Δt and r_0 are found, the resonance removal filter can then be constructed in the frequency domain:

$$F(\omega) = 1 + r_0 e^{-i\omega\Delta t}. \quad (6)$$

The resonance removal filter is applied in the frequency domain by multiplying it with the Fourier transform of the Ps RFs. The reverberations are successfully suppressed from the resulting receiver function, clarifying the later arriving P-to-s Moho phase (Fig. 3b).

Although applying a resonance removal filter makes conversions from the Moho interpretable, it does not correct for the time delay that the Moho-related phases accumulate through the slow sedimentary layer. If the sediment time delay is not corrected when stacking the Ps receiver functions in the *H*–κ–V_P stacks, an incorrect crustal thickness estimate will be obtained (Yeck *et al.* 2013; Yu *et al.* 2015). To address this problem, the Moho phase arrivals used in the *H*–κ–V_P stack can be adjusted for the sediment time delay by using either the P_bs phase arrival, which will be the first large amplitude

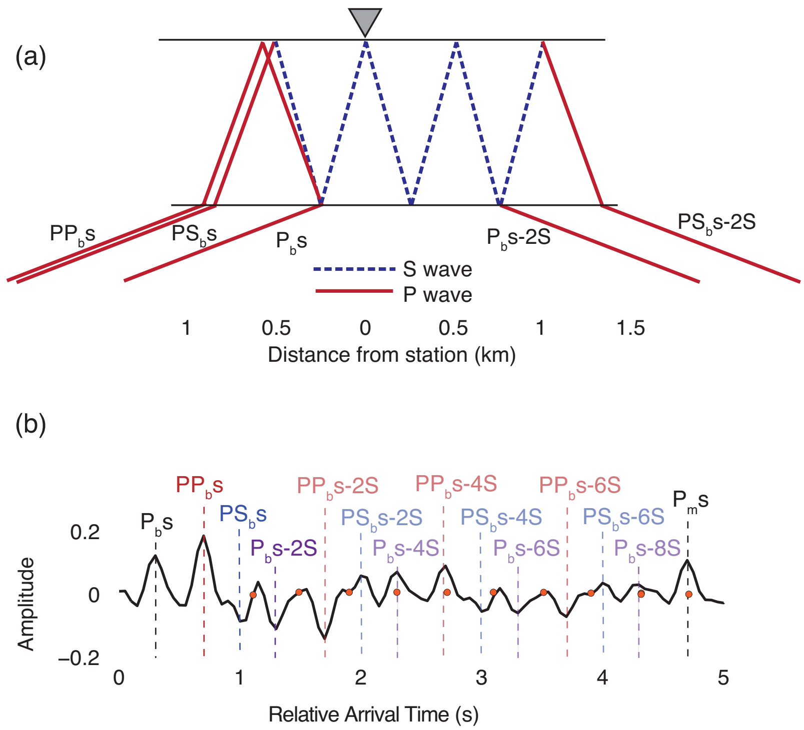

Figure 2. (a) Ray path geometry of P-to-s phases converted across the base of a 0.5-km-thick sediment layer, along with the largest-amplitude first- and second-order multiples for an incident plane wave of horizontal slowness 0.0789 s km^{-1}. (b) Synthetic receiver functions computed for a model with a 0.5-km-thick sediment layer and horizontal slowness 0.06 s km^{-1} ($V_P = 2.5$ km s^{-1}, $V_S = 1$ km s^{-1}), crustal $V_P = 6.2$ km s^{-1}, $V_S = 3.5$ km s^{-1}, a Moho at 35 km depth, and mantle $V_P = 8$ km s^{-1}, $V_S = 4.6$ km s^{-1}. Direct conversions are in black, while the oscillatory pattern is attributed to sediment multiples, labelled in red, blue and purple. Orange dots indicate where the expected arrival of phases with more than 2 *P*-wave legs in the sediment would arrive.

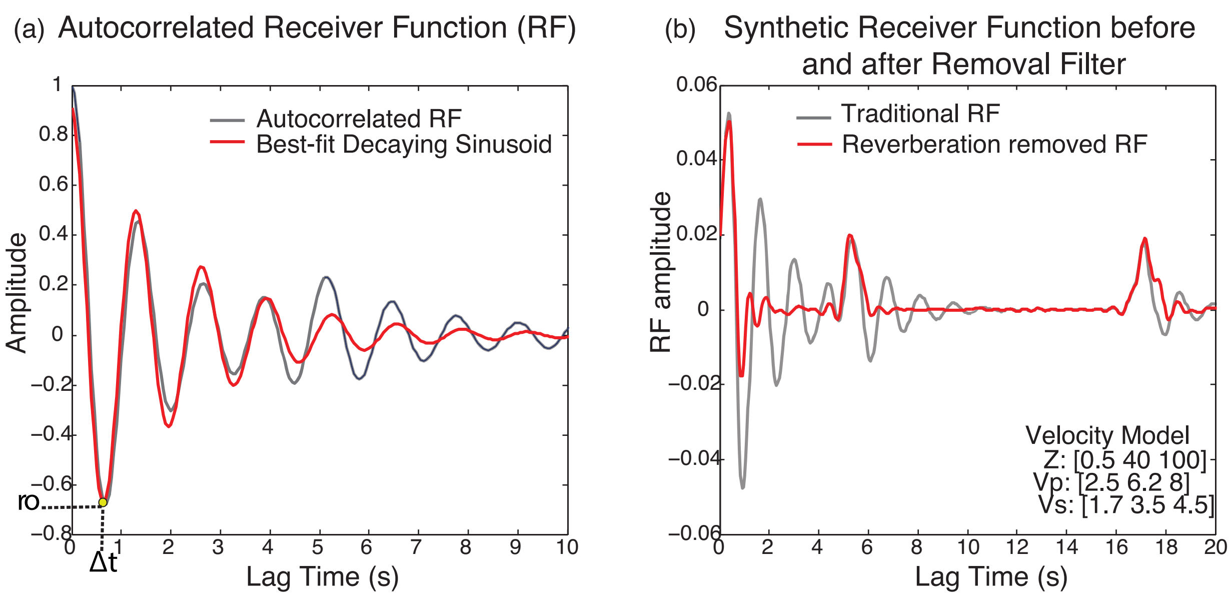

Figure 3. (a) The autocorrelation of the mean synthetic receiver function (grey) and the best-fitting decaying sinusoid (red) used for determining the parameters of the resonance removal filter. The first large amplitude negative peak corresponds to the two-way *S* traveltime in sediment (Δt) on the *x*-axis and the amplitude of the sediment reverberations (r_0) on the *y*-axis. (b) Mean synthetic Ps receiver functions before (grey) and after (red) the resonance removal filter is applied; the filter successfully removes the reverberations and the direct P-to-s conversion across the Moho becomes clear. The velocity model used for computing the synthetic RFs is specified in the.

arrival on the receiver function (Yu *et al.* 2015), or the PP$_b$s phase which is the largest amplitude arrival on the receiver function. The arrival time of the P$_b$s phase (δt) and the PP$_b$s ($\delta t P$) phase can overlap, especially in lower frequency (1 Hz) Ps RFs. It is easiest to identify these phases on high frequency (4 Hz) Ps RFs. Using the high frequency RFs allows for tighter constraints on δt or $\delta t P$ and helps separate the P$_b$s phase arrival from the PP$_b$s phase arrival when the sediment layer is thin (less than 0.5 km). In our automated procedure, we found it was easier to measure the arrival time of the larger phase δtP instead of the first arriving phase δt. Once δtP is determined, the predicted Moho phase arrival times are accounted for in computing the time adjusted H–κ–V_P stack:

$$s_{Ps}(H, \kappa, V_P) = \sum_{j=1}^{N} w_1 f_j \left(t_{P_m s} + \Delta t - \delta tP\right) + w_2 f_j \left(t_{PP_m s} + \delta tP\right) - w_3 f_j \left(t_{PS_m s} + t_{P_m s P_m s} + \Delta t\right). \quad (7)$$

When sedimentary layers are present, eq. (7) corrects for the sediment delay time and yields an estimate of the subsediment crustal thickness. Using the mud-line equation from Brocher (2005), which is appropriate for unconsolidated sediments, a relationship can be assumed between V_P and V_S in sedimentary layers. This relationship can be used to approximate the V_P, V_S and thickness of sedimentary or shallow layer from the measurements of Δt and δtP. To further constrain the crustal thickness and crustal velocity, we add the Sp and SP_mp phase arrivals (Sections 2.4 and 2.5)

2.3 Determining when to correct for sedimentary layers

Applying a sediment removal filter and correcting phase arrival times on the Ps receiver function may introduce error if the data do not exhibit pronounced sediment reverberations. To avoid this, a set of criteria based on quantitative metrics is defined to decide whether the sediment removal filter and arrival time corrections should be applied.

The first criterion that needs to be satisfied for the sediment removal filter to be applied is that the variance of the differences between the sediment removed Ps RF and the original Ps RF (v_1) be larger than the variance of the differences between the autocorrelation of the original Ps RF and the resonance filter (v_2). If v_1 is larger than v_2, the resonance filter fits the autocorrelation of the receiver function well (small v_2) and applying the resonance removal filter changes the resulting RF (large v_1). The second criterion is that the amplitude of the PP_bs arrival, $f(\delta tP)$, is at least 30 per cent of the largest amplitude signal in the receiver function. Alternatively, the sediment removed receiver functions are used if the direct sediment conversion is 90 per cent of the largest amplitude signal in the receiver function, regardless of v_1 or v_2. If the direct sediment conversion is small, the sediment reverberations should not mask deeper arrivals, but if the direct sediment conversion is very large, then reverberations may be overprint deeper signal. If these criteria are met, then the sediment removal filter is applied and delay time corrected to create the SRTC H–κ–V_P stack. By applying a single set of criteria, SRTC H–κ–V_P stacking can be automated for stations across various tectonic/geological settings without having to decide *a priori* whether the station is significantly affected by sediment.

2.4 Sp receiver functions in H–κ–V_P stacks

To further constrain crustal properties beneath a seismic station, it is helpful to add the complimentary Sp receiver function. Like Ps RFs, S-to-p converted waves reverberate between the Moho and the free surface, producing multiples. The S-to-p conversion across the Moho occurs further from the station (Fig. 4) and the *S* wave contains lower frequencies than the *P* wave and so Sp RFs are not used as often as the Ps RFs to constrain crustal properties. However, the Sp phase arrives before the direct *S* wave arrival and is not directly affected by sedimentary layers as the Ps phase. While the direct S_mp conversion across the Moho and its reverberations have been used to constrain crustal thickness and velocity (Rychert & Harmon 2016), we find that signals from sediment multiples arriving immediately after the main *S* phase are difficult to isolate from source–time function complexity and distinguish from the noise; therefore, we choose to only use the direct Sp phase to constrain the crustal thickness.

To compare, and eventually combine, the Sp and Ps RFs the Sp RFs polarity is flipped so that a conversion across an impedance increase with depth corresponds to a positive phase, and then the Sp RF is time-reversed so S_mp phase arrives after the direct *S*. In this convention, the relative arrival time of the direct Sp conversion depends on the crustal thickness (H), crustal velocity (V_P and V_S) and *S*-wave ray parameter (p_{Sp}) in exactly the same way as Ps arrival time (eq. 1). The sum of all Sp receiver functions (N_{Sp}) computed at a station, $f'_j(t)$, and evaluated at the expected arrival times for a range of crustal thickness (H), V_P/V_S ratios (κ) and average crustal V_P yields the expression analogous to eq. (4):

$$s_{S_m p}(H, \kappa, V_P) = \sum_{j=1}^{N_{Sp}} f'_j \left(t_{S_m p}\right). \quad (8)$$

If the Ps RFs indicate the presence of a sufficiently thick shallow layer (see Section 2.3), the delay time of the converted *P* wave in sediment compared to the direct *S* wave is estimated to be $\Delta t - \delta tP$ by assuming vertical incidence in the sediment. When constructing the Sp H–κ–V_P stack, we correct for the delay time of the *P* wave in sediment as:

$$s_{S_m p}(H, \kappa, V_P) = \sum_{j=1}^{N_{Sp}} f'_j \left(t_{S_m p} + \Delta t - \delta tP\right). \quad (9)$$

Stacking the direct S_mp conversions on their own does not result in a maximum at a single, optimal H–κ–V_P combination; rather, $s_{S_m p}$ yields a range of possible H, κ and V_P values. This is nevertheless beneficial because traditional Ps RF H– κ stacks with noisy data can be characterized by spurious maxima arising from constructive interference of noise or multiples that do not correspond to correct crustal H and κ values. Therefore, in addition to helping to constrain V_P, the strength of including the complementary Sp stack is that it significantly restricts the range of possible maxima, especially regarding crustal thickness (H). To further improve the ability to determine crustal thickness, V_P/V_S, and especially average crustal V_P, constraints from the SP_mp conversion are incorporated.

2.5 SP_mp receiver functions in H–κ–V_P stacks

The SP_mp phase provides constraints complementary to those from Sp and Ps RFs since it is sensitive to crustal thickness and average crustal V_P. The SP_mp phase involves a post-critical reflection of the *P* wave at the Moho which is produced when ray parameters of incoming teleseismic *S* waves are sufficiently large, and are greater than the maximum ray parameters used in constructing typical Sp stacks (e.g. Wilson *et al*. 2006). As a result, the horizontal location of the conversion point is far away from the station (>50 km, Fig. 5). The raw SP_mp waveform contains complexity due to the earthquake source–time function and source-side propagation effects. Therefore, just as for the Sp RF, these source effects are suppressed by deconvolving the parent (*S*) component from the daughter component (*P*) and computing an SP_mp receiver function. Unlike the direct Sp phase, SP_mp arrives after the direct *S* wave, and so it can be combined with the Ps RF without being flipped in time. Despite arriving after the direct *S* wave, the SP_mp RF is less sensitive to sediment reverberations (Parker *et al.* 2016). In regions where the assumed average crustal V_P is inaccurate and sedimentary layers

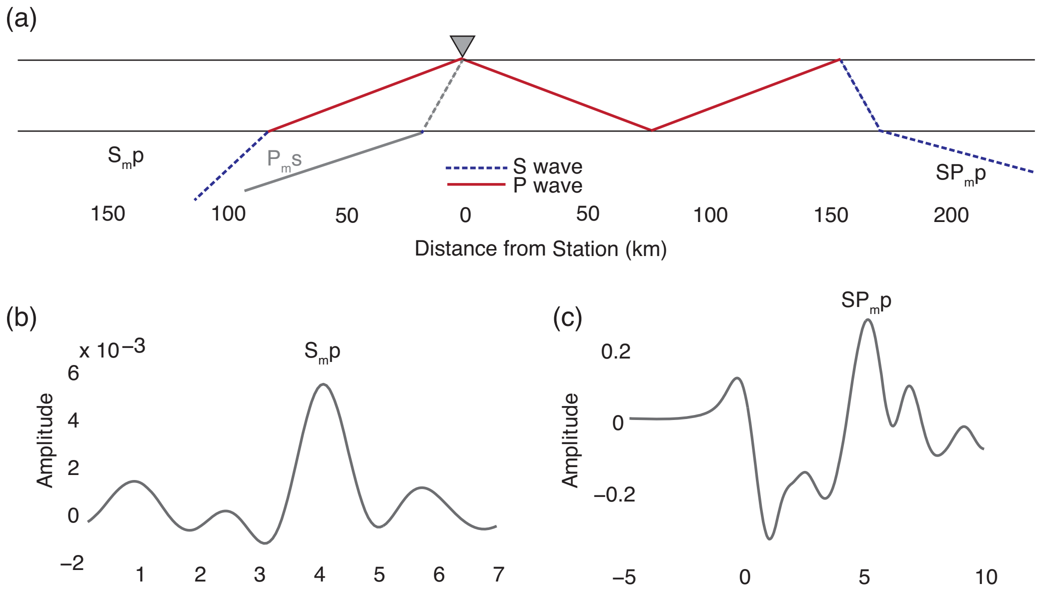

Figure 4. (a) Ray path geometry of S to p converted phases across the Moho at 30 km depth calculated for an incident plane wave of 0.14 s km^{-1} and the post critical *P* wave reflection across the 30 km deep Moho (SP_mp) with incident plane wave of 0.1486 s km^{-1}. The Ps conversions from the Moho are plotted for comparison (grey line). (b) Synthetic receiver function of the S-to-p phases converted across the Moho. Time is relative to the direct *S* arrival (positive values indicate earlier arrivals). (c) Synthetic receiver function of the Hilbert-transformed post-critical *P* phase at the Moho. Time is relative to the direct *S* arrival (positive values indicate later arrivals). Crustal $V_P = 6.3$ km s^{-1}, $V_S = 3.7$ km s^{-1}, while mantle $V_P = 8$ km s^{-1} and $V_S = 4.6$ km s^{-1}.

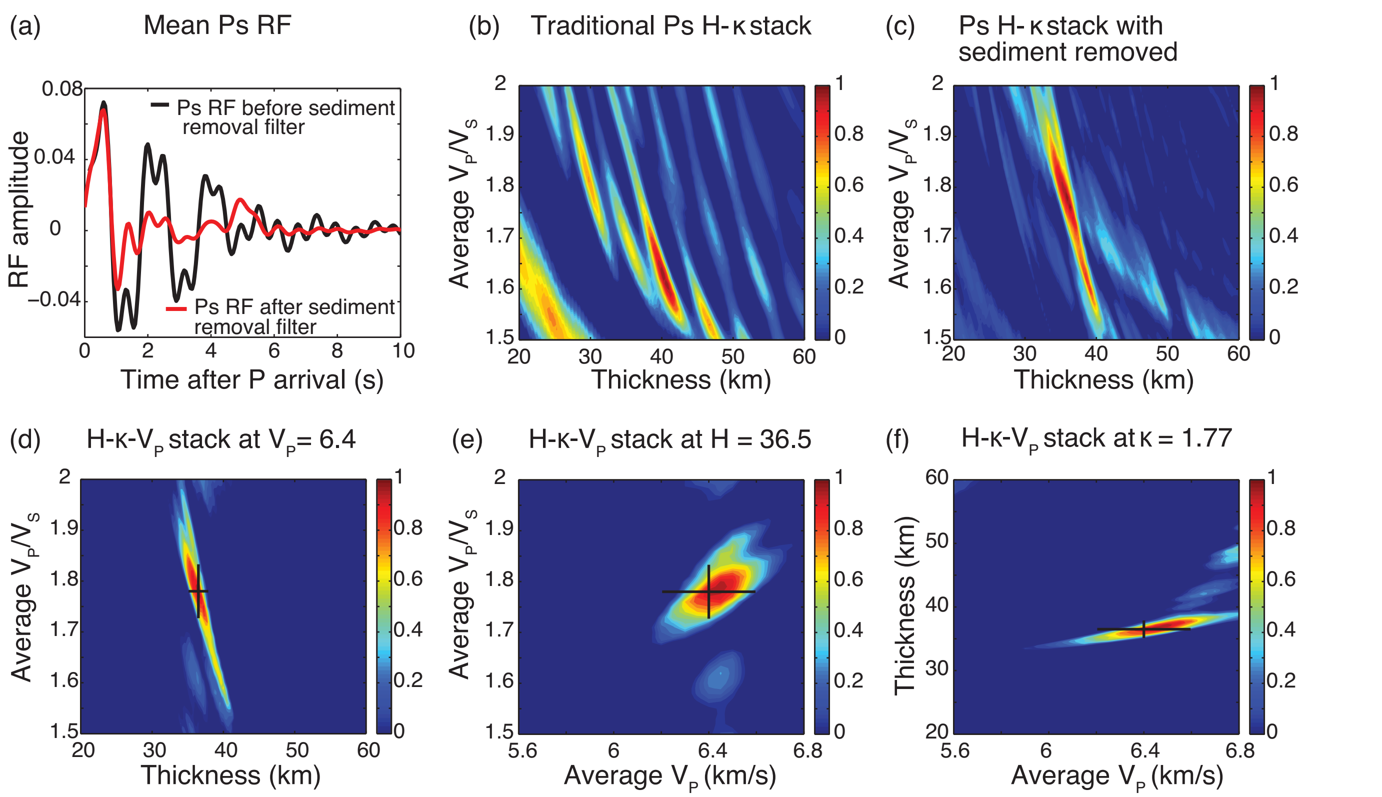

Figure 5. SRTC H–κ–V_P stacking of synthetic receiver functions, where negative values in the stack are clipped. Input model has a 0.5-km-thick sedimentary layer, V_P of 2 km s^{-1}, and $\kappa = 2.3$, and a Moho at 37 km depth with crustal $V_P = 6.3$, and $\kappa = 1.76$. (a) The mean Ps receiver function before (black) and after (red) the sediment removal filter is applied. (b) Ps H–κ stack at assumed $V_P = 6.3$ shows no clear maxima. (c) The Ps H–k stack after the sediment removal filter and time correction is applied shows a clear maximum. (d, e and f) Three cross-sections through the maximum of the H–κ–V_P triple stack; black cross hairs denote 1σ error bars.

may mask Moho signals on the Ps RF, the large amplitude SP_mp phase has proven useful in obtaining crustal thickness estimates (e.g. Langston 1996; Owens & Zandt 1997; Yu *et al.* 2012; 2015; Parker *et al.* 2013; 2016; Tian *et al.* 2015; Kang *et al.* 2016).

The SP_mp RF should not be directly incorporated into a H–κ–V_P stack because the post-critical reflection produces phase shifts that result in waveform distortion. These distortions are removed by computing the envelope of each SP_mp receiver function (Bracewell 1968). The expected phase arrival time of the SP_mp conversion relative to the direct S wave arrival depends only on H, V_P and the ray parameter, p_{SsPmp}:

$$t_{SsP_mp} = 2H\sqrt{{V_P}^{-2} - {p_{SsP_mp}}^2}. \quad (10)$$

Because the post critical P wave reflection occurs for events within a small range of epicentral distances, fewer data are available for SP_mp RFs than for Ps and Sp RFs. To suppress bias due to noise, we phase weight stack the SP_mp RFs (Schimmel & Paulssen 1997), yielding a set of $f_j^{''}(t)$ that help ensure that the SP_mp RFs are accurate. As with Sp and Ps RFs, a H–κ–V_P stack can be constructed by summing all available $f_j^{''}(t)\,(N_P)$ at expected arrival times, t_{SsPmp} eq. (10), for a range of H, κ and V_P values:

$$s_{SsP_mp}\ (H, \kappa, V_P) = \sum\nolimits_{j=1}^{N_P} f_j^{''}\left(t_{SsP_mp}\right). \quad (11)$$

Note that this stack is identical for all values of κ. If the analysis of Ps receiver functions indicates that sediment corrections are necessary (see Section 2.3), the SP_mp traveltime is corrected by again assuming vertical incidence within the sedimentary layer. The time-corrected H–κ–V_P stack is given by:

$$s_{SsP_mp}\ (H, \kappa, V_P) = \sum\nolimits_{j=1}^{N_P} f_j^{''}\left(t_{SsP_mp} + 2\delta t P - \Delta t\right). \quad (12)$$

The additional constraints provided by the SP_mp RFs, when combined with Ps and Sp stacks, will allow us to constrain V_P, as well as H and κ beneath a seismic station even when thick sediment layers are present.

2.6 Calculating combined SRTC H–κ–V_P stacks with error

The final step in creating the SRTC H–κ–V_P triple stack is to determine the best method to combine the Ps, Sp and SP_mp SRTC H–κ–V_P stacks and quantify error. Each stack is normalized by its absolute maximum (denoted by the overbar), and the triple stacks (Ps, Sp and SP_mp) are combined by adding them to create a joint SRTC H–κ–V_P triple-stack:

$$s\,(H, \kappa, V_P) = \overline{sPs\,(H, \kappa, V_P)} + \overline{sSp\,(H, \kappa, V_P)} + \overline{sSP_mp\,(H, \kappa, V_P)}, \quad (13)$$

where the absolute maximum of the stack will be the best-fitting H, κ and V_P crustal parameters to the Ps, Sp and SP_mp RFs. This volumetric stack can be visually represented on three planes cutting through the maximum of the triple stack (see Fig. 5).

To quantify the uncertainty of the estimates of optimal H, κ, V_P values, we look at the spread of the stack amplitude along its three axes. The stack amplitude is interpreted as proportional to log-likelihood. Therefore, ignoring higher order terms of the Taylor series expansion of the stack around the maximum, the curvature of the stack can be related to the posterior covariance matrix representing uncertainty of our parameter estimates. Specifically, the posterior covariance matrix is given by the negative inverse of the second-derivatives matrix evaluated at the triple stack maximum (Sivia 2006):

$$\begin{bmatrix} \sigma_H^2 & \sigma_{HV_P}^2 & \sigma_{H\kappa}^2 \\ \sigma_{HV_P}^2 & \sigma_{V_P}^2 & \sigma_{V_P\kappa}^2 \\ \sigma_{H\kappa}^2 & \sigma_{V_P\kappa}^2 & \sigma_\kappa^2 \end{bmatrix} = -\begin{bmatrix} \dfrac{d^2s}{dH^2} & \dfrac{d^2s}{dHdV_P} & \dfrac{d^2s}{dHd\kappa} \\ \dfrac{d^2s}{dHdV_P} & \dfrac{d^2s}{d{V_P}^2} & \dfrac{d^2s}{dV_Pd\kappa} \\ \dfrac{d^2s}{dHd\kappa} & \dfrac{d^2s}{dV_Pd\kappa} & \dfrac{d^2s}{d\kappa^2} \end{bmatrix}^{-1}, \quad (14)$$

where s is the triple stack (from eq. 13) amplitude at the optimal H, κ, V_P values. The original paper introducing the H–κ stacking method (Zhu & Kanamori 2000) proposed calculating the uncertainty of H and κ estimates made from the stack by dividing stack variance by the second derivative for H and κ, which ignores the covariance terms. This corresponds to computing the uncertainty on each parameter at the preferred value of the other parameter(s). Due to trade-offs among parameters captured in the off-diagonal terms of the covariance matrix, however, this estimate is a lower bound on the true uncertainty. The uncertainty estimates represented by the variances in eq. (14), on the other hand, are a more appropriate measure of uncertainty since they capture additional uncertainty arising from our ignorance about the true values of the other parameters. It should be noted that even for traditional H–κ stacks, the error should be calculated including the covariance terms.

3 DATA

We evaluate the effectiveness of the H–κ–V_P stacking method for constraining crustal V_P, V_P/V_S and thickness using synthetic receiver functions as well as data recorded at three EarthScope Transportable Array (TA) stations, which span various geological and tectonic settings, but all suffer from shallow layer contamination. The stations are: (1) B30A located in Edmore, ND on the eastern edge of the Williston basin; (2) 448A in Bay Minette, AL located within the Mississippi embayment and (3) U60A in Pendleton, NC within the Atlantic coastal plain (ACP).

To calculate Ps RFs for each station, we obtain 300 s three-component waveforms around the P arrival time for events with $M_w > 5.6$ at epicentral distances between 30° and 90° from the station. (Abt *et al.* 2010). Sp receiver functions are further restricted to events with epicentral distances between 55° and 90° and source depths less than 300 km (Wilson *et al.* 2006). SP_mp waveforms are restricted to events with epicentral distances between 30° and 50° (Yu *et al.* 2013). A summary of the number of Ps, Sp and SP_mp events, along with the slowness range for each station is shown in Table S1.

The automatic quality-control procedure is detailed in Abt *et al.* (2010). In this study, we culled the dataset to have a minimum Z-to-R cross correlation of 0.3, and a maximum difference of 25 s between the automatically determined arrival time and prediction for ak135. While we did not use an additional signal-to-noise threshold for the Ps and Sp RFs, for SP_mp RFs we require that the Hilbert transform of the SP_mp arrival is greater than 1.2 of the S-wave arrival amplitude. We follow the Abt *et al.* (2010) procedure for calculating RFs, using a free-surface transform matrix (Kennett 1991) and finding the surface velocity that minimizes the parent amplitude (P for Ps and S for Sp) on the daughter component to project the waveforms onto the P-SV-SH system, pick the arrival times, and apply a fourth order Butterworth bandpass filter to waveforms of 0.03–1 Hz and 0.03–4 Hz for Ps, and 0.03–0.5 Hz for both Sp and SP_mp. We then use the iterative time domain deconvolution with Gaussian half-amplitude half-width of ∼0.12, ∼0.5 and ∼1 s for 4, 1 and 0.5 Hz, respectively, to calculate the receiver functions (Ligorria & Ammon 1999).

To compute synthetic receiver functions, synthetic seismograms are generated using the flat-layer reflectivity algorithm ANIREC (Levin & Park 1997) for a range of slowness and backazimuth. Then, a fourth-order Butterworth bandpass filter is applied to waveforms (0.03–1 Hz or 0.03–4 Hz for Ps, and 0.03–0.5 Hz for both Sp and SP_mp) and the parent waveform is deconvolved from the daughter waveform using iterative time domain deconvolution (Ligorria & Ammon 1999), which we have found to yield smaller side-lobes than frequency domain deconvolution.

We calculate the triple stacks over a range of possible crustal H, κ and V_P, values where H ranges from 20 to 60 km, κ ranges from 1.5 to 2, and V_P ranges from 5.6 to 6.8 km s^{-1}.

4 RESULTS AND OBSERVATIONS

The results of SRTC H–κ–V_P stacking applied to synthetic waveforms and three EarthScope TA stations with a low velocity sediment layer are presented. The estimates of crustal thickness before and after the SRTC H–κ–V_P stacking method is used are compared and the results are also compared to crustal thickness estimates in these regions from previous studies.

Because time corrections are made to each phase to account for the slow sedimentary layer, the average crustal thickness, V_P/V_S and V_P at each station will correspond to the crust below the sediment. To determine the Moho depth from our study and compare with other studies, the thickness of the sediment should be added to the crustal thickness estimates from the SRTC H–κ–V_P stacks. The sediment thickness is estimated at each station using the measurements of Δt and $\delta t P$ and assuming a relationship of V_P and V_S relationship from the mud-line equation (Brocher 2005). In general, the sediment thickness found using Δt and $\delta t P$ agrees within 0.1 km of the shallowest sediment layer from the CRUST 1.0 model (Laske *et al.* 2013). We interpret this shallowest layer of sediment as the unconsolidated sediment thickness at each station. At station TA B30A, we find a sediment thickness of 0.38 km, which agrees with estimates of 0.3–0.5 from multiple datasets (AAPG 1967; Laske *et al.* 2013). At station U60A we find a sediment thickness of 0.28 km, similar to the estimate of 0.3 km interpolated from drill hole data using Bouger gravity maps (Lawerence & Hoffman 1993). but much smaller than the estimate from Crust 1.0 of 0.9 km (Laske *et al.* 2013), but much thicker than the estimate of 0.3 km interpolated from drill hole data using Bouger gravity maps (Lawerence & Hoffman 1993). This discrepancy in sediment thickness values at U60A could arise from differences in interpreting what constitutes the shallowest sedimentary layer; alternatively, they could be due to differences in the velocity used to determine the thickness of the sedimentary layer. Finally, at station TA 448A we calculate a sediment thickness to be 0.64 km, is similar to estimates of 0.6 km from CRUST 1.0 (Laske *et al.* 2013) and deeper than the estimate of 0.339 kmfor nearby station Y46A from horizontal to vertical ambient noise measurements (Langston & Horton 2014). However, at station 448A the depth to basement is between 4 and 6 km thick (AAPG 1967) and so we expect that there are multiple basin layers beneath this 0.64-km-thick layer. Tighter constraints and better uncertainty estimates can be achieved by either using higher frequency receiver functions (e.g. Leahy *et al*. 2012) or by stacking receiver functions for predicted sedimentary multiples (e.g. Sheehan *et al.* 1995). However, since the goal of this study is accurate estimates of total crustal thickness, the rough estimation of sediment thickness from the travel time is sufficient, as the uncertainty of the resulting crustal thickness estimates are smaller than those achievable with the H–κ–V_P stacking method.

4.1 SRTC H–κ–V_P stacking with synthetic waveforms

The model used for calculating the synthetic waveforms has a sedimentary layer of thickness (H) of 0.5 km, V_P of 2.3 km s^{-1} and κ of 2.1 underlain by 36.5-km-thick layer more representative of crystalline rock, with $V_P = 6.4$ km s^{-1} and $\kappa = 1.76$. Before carrying out H–κ–V_P stacking, how the application of the sediment removal filter affects the appearance of mean Ps RFs relative to the results of traditional H–κ stacking is compared. (Figs 5a–c).

The mean Ps RF computed from the synthetic waveforms is dominated by large amplitude sediment reverberations (black line, Fig. 5a). After the sediment reverberation removal filter is estimated and applied (eq. 6), the mean Ps RF shows one clear arrival at ∼5 s (red line, Fig. 5a) corresponding to the Ps conversion across the Moho, but which was masked by sediment reverberations before the application of the resonance removal filter.

Ps RFs computed with and without the resonance removal filter yield dramatically different results when used for traditional and SRTC H–κ stacking, respectively. To illustrate this, traditional H–κ stacks computed using the original Ps RFs are plotted (black line–Fig. 5a) and compared to SRTC H–κ stacks computed using the resonance removed Ps RFs (red line–Fig. 5a) at an assumed crustal V_P of 6.3 km s^{-1}. While the traditional Ps H–κ stack shows no clear Moho maximum (Fig. 5b), one might be interpreted at $H = 42$ km and $\kappa = 1.63$ (Fig. 5b). SRTC H–κ stacks, on the other hand, show a much stronger maximum at $H = 37$ km and $\kappa = 1.79$ (Fig. 5c), which is nearly identical to the model values used to calculate the synthetic waveforms.

Having validated that the SRTC H–κ stacks are much better at resolving the input crustal structure in the presence of a shallow low-velocity layer, complementary Sp RFs are added, because they are not contaminated by sediment reverberations (Farra & Vinnik 2000). If the sediment removal filter is not successful in removing all of the reverberations or if there are multiple basin layers with phase arrivals overprinting Moho arrivals, the Sp H–κ–V_P stacks can help clarify crustal thickness. Finally, the SP_mp RFs are introduced to remove the dependence on an assumed average crustal V_P and better constrain the crustal thickness (H). A combined SRTC H–κ–V_P stack is computed (eq. 13) for the same input model by adding the weighted time-corrected Sp (eq. 9) and SP_mp (eq. 12) RFs to the SRTC Ps stacks, Fig. 5. Unlike H–κ stacking, which can be fully visualized on a 2-D contour plot, the H–κ–V_P stack varies in amplitude along three axes; therefore, slices through the stack volume are shown. In Fig. 5(d), when the Sp and SP_mp RFs are added, again there is one clear maximum in the SRTC H–κ–V_P stack (Figs 5d and e). The crustal parameters are $H = 41.25 \pm 2$ km, $V_P = 6.3 \pm 0.3$ km s^{-1} and $\kappa = 1.75 \pm 0.09$.

To investigate the dependence of the SRTC H–κ–V_P stacking results on noise, this analysis is repeated for increasing amounts of noise (we filter random white noise to have similar frequency content as typically encountered noise) with the maximum amplitude of the noise being 75 per cent of the maximum amplitude of the daughter waveform (P for Sp and S for Ps) added to all of the waveform components. The H, κ and V_P values of the input model within error are still able to be resolved (Fig. S4). This illustrates the ability of the SRTC H–κ–V_P stack to resolve the three crustal parameters from synthetic waveforms persists even under realistic noise levels.

It also demonstrates that when a sedimentary layer is present, the sediment-removed, time-corrected Ps RFs, time-corrected Sp RFs, and time-corrected SP_mp are all needed to constrain parameters in the Ps H–κ–V_P stacks. Additionally, the sediment thickness is roughly estimated to be $H = 0.5$ km, which is consistent with the input sediment thickness value. Therefore, both the sediment and the crustal structure of the synthetic model are successfully retrieved using the SRTC H–κ–V_P stacking method.

4.2 TA station B30A: eastern Williston Basin

Having validated the SRTC H–κ–V_P stacking method on synthetics, it is applied to data recorded at a station where reverberations from shallow sediments can be expected. EasrthScope Temporary Array (TA) station B30A lies on the eastern edge of the Williston basin in northeastern Montana. The Ps RFs were calculated using the best-fitting free-surface transform velocities of $V_P = 5.3$ km s^{-1} and $V_S = 2.9$ km s^{-1}. The estimated V_P and V_S for this station (along with the following two stations) are quite reasonable, providing confidence that the free-surface transform is successful. The measurement of $\delta t P$ is made on the 4 Hz Ps RFs (Fig. S5) and is 0.6 s. The measurement of Δt at station B30A is 1.17 s and is measured from the autocorrelation of the 1 Hz Ps RF. There no difference between the 1 and 4 Hz RF for this measurement (Fig. S5). The Ps RF before the sediment removal filter is dominated by large amplitude, oscillatory signals due to *S*-wave reverberations within the low velocity shallow layer (black line, Fig. 6a, Fig. S8). From the measurements of Δt and $\delta t P$, sediment thickness is estimated to be 0.38 km. The traditional Ps H–κ stack has a maximum at $H = 28.5$ km and $\kappa = 1.62$ (Fig. 6b), which would suggest anomalously thin crust and a crustal V_P/V_S representative of quartz sandstone (>57 per cent SiO_2) to the base of the crust (Christensen 1996). After the sediment removal filter is applied to the Ps RFs, the amplitude of the receiver function decreases with increasing lagtime (red line–Fig. 6a), and the oscillatory behaviour is suppressed. The SRTC Ps H–κ stack shows a stronger maximum, indicative of a better fit to the direct conversions and multiples, which occurs at a greater depth, $H = 40$ km and a higher V_P/V_S, $\kappa = 1.77$ (Fig. 6c). When complimentary Sp and SP_mp RFs are added to create a SRTC H–κ–V_P stack, the maximum occurs at $H = 44.25 \pm 2.63$ km, $V_P = 6.75 \pm 0.43$ km s^{-1} and $\kappa = 1.76 \pm 0.09$. (Figs 6d and e). By applying the SRTC H–κ–V_P triple stacking method to this station, a thicker continental crust is found with a more realistic average V_P/V_S—consistent with a generally more mafic crustal composition (e.g. diorite or amphibolite per Christensen 1996) compared to traditional H–κ stacking, and estimate average crustal V_P instead of having to assume it *a priori*.

Previous studies near the location of TA station B30A estimate the Moho depth to be between 38 and 45 km (Cook *et al.* 1981; Langston 1994; Chulick & Mooney 2002). Those values agree within error with our estimate for crustal thickness of 44.25 ± 2.63 km (or a Moho depth of 44.73 km). However, the EarthScope Automated Receiver Survey (EARS), which uses a modified version of the traditional H–κ stack, finds a much lower estimate for the crustal thickness of 30 ± 5.8 km (Crotwell & Owens 2005). The V_P/V_S (κ) from the SRTC H–κ–V_P triple stack is 1.76 ± 0.09, while the EARS estimate of κ is much lower at 1.65 ± 0.07. The likely explanation for the inconsistency between these two results is that by implementing the sediment removal filter and adding Sp and SP_mp stacks, the amplitude of the shallower maximum is reduced (Fig. 6b) and the deeper maximum is highlighted. (Figs 6c–f). The average crustal *P*-wave velocity (V_P) of 6.75 ± 0.43 km s^{-1} is consistent within error of previous results where the velocity is between 6.53 and 6.6 km s^{-1} (Langston 1994; Chulick & Mooney 2002; Laske *et al.* 2013) and agrees with the higher V_S found under the Williston Basin by Schulte-Pelkum *et al.* (2017). The consistency of the three crustal parameters with previous studies gives us confidence that the H–κ–V_P triple stacking method is valid in this region.

4.3 TA station U60A: Atlantic coastal plain

Due to shallow sedimentary layers, one particularly challenging region for receiver function interpretation has been the Atlantic coastal plain. EarthScope TA station U60A lies on the eastern North Carolina portion of the Atlantic coastal plain. The Ps RFs were calculated using the best-fitting free-surface transform velocities of $V_P = 6$ km s^{-1} and $V_S = 3.4$ km s^{-1}. The measurement of $\delta t P$ is made on the 4 Hz Ps RFs (Figs S6a and S8) and is 0.2 s. The measurement of Δt at station U60A is 0.8 s and is measured from the autocorrelation of the 1 Hz Ps RF. We note a slight difference between the Δt obtained from the 1 and 4 Hz RF autocorrelations at this station (Fig. S6b). The Ps RF before the sediment removal filter for station U60A has a large amplitude oscillatory signal at lag times <5 s due to shallow layer reverberations (black line, Fig. 7a). From the measurements of Δt and $\delta t P$, the sediment thickness is estimated to be 0.28 km and calculate a sediment removal filter. When the filter is applied to the Ps RFs, the amplitude of the early arriving oscillatory phases is reduced and a peak appears in the sediment removed Ps RF (red line, Fig. 7a) at approximately 4 s. In the traditional Ps H–κ stack calculated with the Ps RFs before the resonance removal is applied, no clear maxima appear deeper than 20 km (Fig. 7b), and no realistic constraint on crustal thickness and V_P/V_S can be placed. However, when the SRTC Ps H–κ stack calculated with the resonance removed Ps RFs, a deeper maximum becomes clear at $H = 30.5$ km and $\kappa = 164$. When the time-corrected Sp and SP_mp RFs are incorporated in the SRTC H–κ–V_P triple stack, a maximum is found at $H = 31.75 \pm 2.28$ km, $V_P = 6.0 \pm 0.38$ km s^{-1} and $\kappa = 1.65 \pm 0.09$ (Figs 7d and e), which suggests thinner and slower average crust than that present beneath the Williston basin, The sediment removal filter and the SRTC H–κ–V_P triple stack allows meaningful constraints to be placed on average crustal properties. Even when the sediment multiples completely mask the crustal signal in the Ps RF; the SRTC H–κ–V_P stack finds a reasonable maximum associated with the crust where none existed in the traditional H–κ stack.

Most regional and active source studies of the Atlantic coastal plain that directly interpret their results in terms of the geology have taken place further south than TA U60A. There is a slight disagreement on the Moho depth in on the Atlantic coastal plain, where the Moho depth may be shallower, between 30 and 35 km (Cook *et al.* 1981; Chulick & Mooney 2002; Li 2002; Abt *et al.* 2010; Laske *et al.* 2013; ; Parker *et al.* 2016), or deeper, between 35 and 40 km (Crotwell & Owens 2005; Lynner & Porrit 2017). We find the crustal thickness at station U60A to be thin 31.75 ± 3.52 km (a shallow 32.03 km Moho depth), in agreement with the first set of studies. We find a low with a V_P/V_S (κ) of 1.65 ± 0.17 which agrees within error with estimates of V_P/V_S between 1.69 and 1.72 in the Atlantic coastal plain (Musacchio *et al.* 1997; Parker *et al.* 2013). We also find a slow average crustal V_P of 6.0 ± 0.79 km s^{-1} compared to some studies which estimate that $V_P = 6.4$–6.7 km s^{-1} (Laske *et al.* 2013) but that agrees with previous studies, which suggests the crustal *P*-wave velocity is between 6.0 and 6.5 km s^{-1} (Chulick

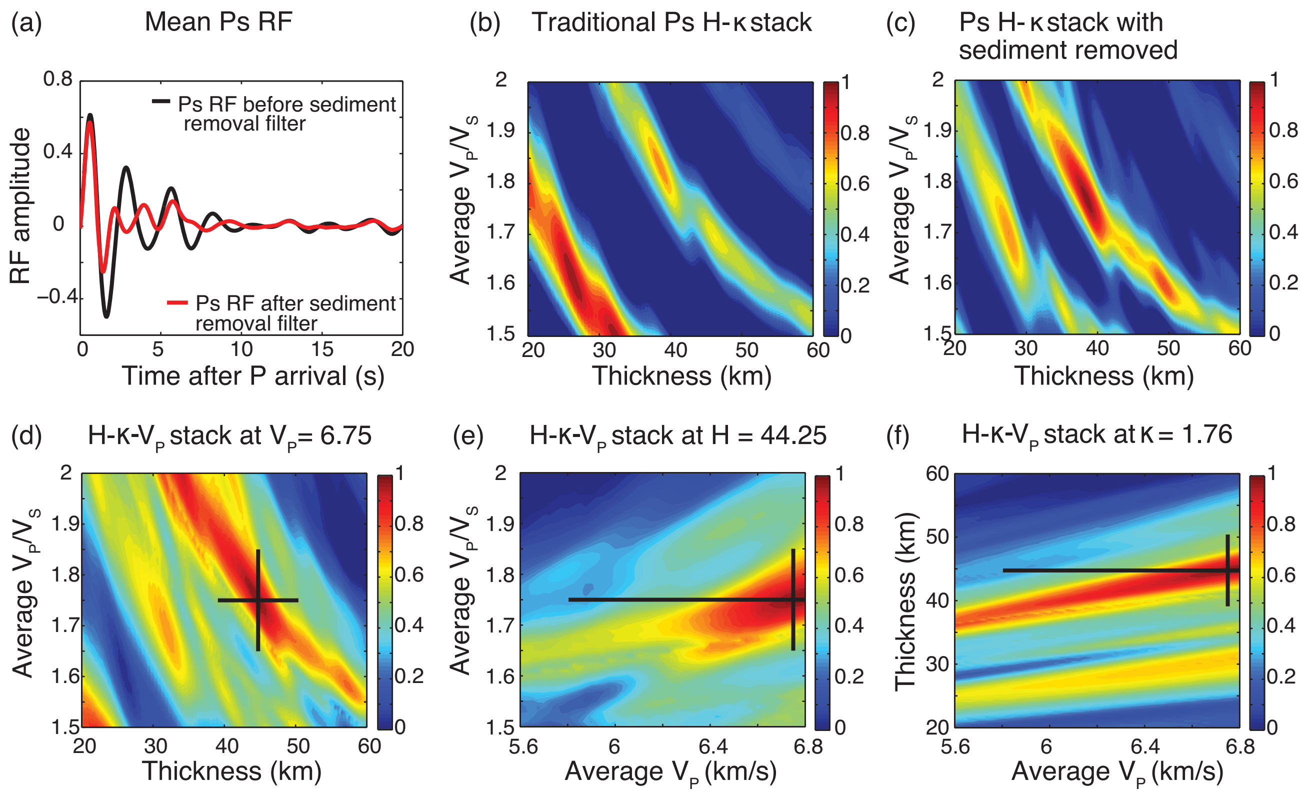

Figure 6. SRTC H–κ–V_P stacking of B30A receiver functions, where negative values in the stack are clipped. Station B30A is located on the eastern edge of the Williston Basin in Montana. (a) The mean Ps receiver function before (black) and after (red) the sediment removal filter is applied. (b) Ps H–κ stack at assumed $V_P = 6.3\,\mathrm{km\,s^{-1}}$ shows a maximum of the stack at $H = 28.5$ km and $\kappa = 1.62$. (c) The Ps H–κ stack after the sediment removal filter and time correction is applied; the stack maximum now corresponds to larger H and κ values (d, e and f) Three cross-sections through the maximum of the H–κ–V_P triple stack; black cross-hairs denote 1σ error bars.

& Mooney 2002). The large error of the V_P estimate means that SRTC triple-stacking at this station is not able to precisely resolve the average *P*-wave velocity at this station.

4.4 TA station 448A: Mississippi embayment

The final station on which SRTC H-κ-V_P triple stacks is calculated is EarthScope TA station 448A, located within the lower Mississippi embayment. The Ps RFs were calculated using the best-fitting free-surface transform velocities of $V_P = 5.9\ \mathrm{km\,s^{-1}}$ and $V_S = 3.2\ \mathrm{km\,s^{-1}}$. The measurement of $\delta t P$ is made on the 4 Hz Ps RFs (Fig. S7A) and is 0.85 s. The measurement of Δt at station 448A is 2.2 s and is measured from the autocorrelation of the 1 Hz Ps RF. However, while there is little difference between the 1 and 4 Hz RF for this measurement (Fig. S7b), we do see two negative peaks in the 4 Hz autocorrelation, which implies either that there are remaining high frequency effects from remaining P-multiples, or more likely that there are multiple sedimentary layers beneath station 448A given what is known about the geological setting. From the measurements of Δt and $\delta t P$ the sediment thickness is estimated to be 0.64 km at this station. Unlike the two previous stations, applying the sediment removal filter at 448A does not significantly change the amplitude or arrival time of phases in the mean Ps RFs (red line compared to black line, Fig. 8a, Fig. S8). Therefore, one might expect that the traditional and SRTC Ps H–κ stacks would be similar to SRTC stacks. Nevertheless, this is not the case, as implementing the time corrections (eq. 7) significantly changes the coherence in the SRTC H–κ stacks. While the traditional H–κ stack has a maximum at $H = 22$ km and $\kappa = 1.5$ (Fig. 8b), the SRTC Ps H–κ stack (Fig. 8c) has a deeper maximum at $H = 35.5$ km and $\kappa = 1.67$. While the sediment time corrections applied to the Ps RFs have a significant effect on improving the coherence, the multiple sediment layers that likely exist beneath station 448A introduce complex signals that prevent the elucidation of the direct Moho conversion $P_m s$. Station 448A provides a good example on how the Sp and $SP_m p$ RFs can improve the interpretation of crustal values in a region with multiple sediment layers. When time-corrected Sp and $SP_m p$ RFs are incorporated, the crustal properties corresponding to the maximum of the SRTC H–κ–V_P triple stack are $H = 39.5 \pm 2.39$ km, $V_P = 6.5 \pm 0.29\,\mathrm{km\,s^{-1}}$ and $\kappa = 1.65 \pm 0.08$. (Figs 8d and e). Station 448A highlights the importance of applying time corrections when calculating the H–κ stack in the presence of a low velocity shallow layer, even if the Ps RFs remain similar before and after the sediment removal filter is applied.

Several previous studies of the lower Mississippi embayment near the location of TA station 448A find similar results to the crustal values obtained in the SRTC H–κ–V_P triple stacks. In southern Mississippi (slightly further west than station 448A) the Moho depth was found using seismic refraction to be ~35 km with an average crustal V_P of 6.4 $\mathrm{km\,s^{-1}}$ (Warren *et al.* 1966), shallower than the SRTC H–κ–V_P stack crustal thickness estimate of 39 km. A global Moho study finds that the Moho depth in this region is between 32 and 36 km with an average crustal V_P of 6.5 $\mathrm{km\,s^{-1}}$ (Cook *et al.* 1981; Mooney *et al.* 1983). Finally, while there are no EARS results for station 448A, the results for a nearby station, US BRAL, finds a Moho depth of 38 km, a V_P/V_S of 1.87, assuming an average crustal

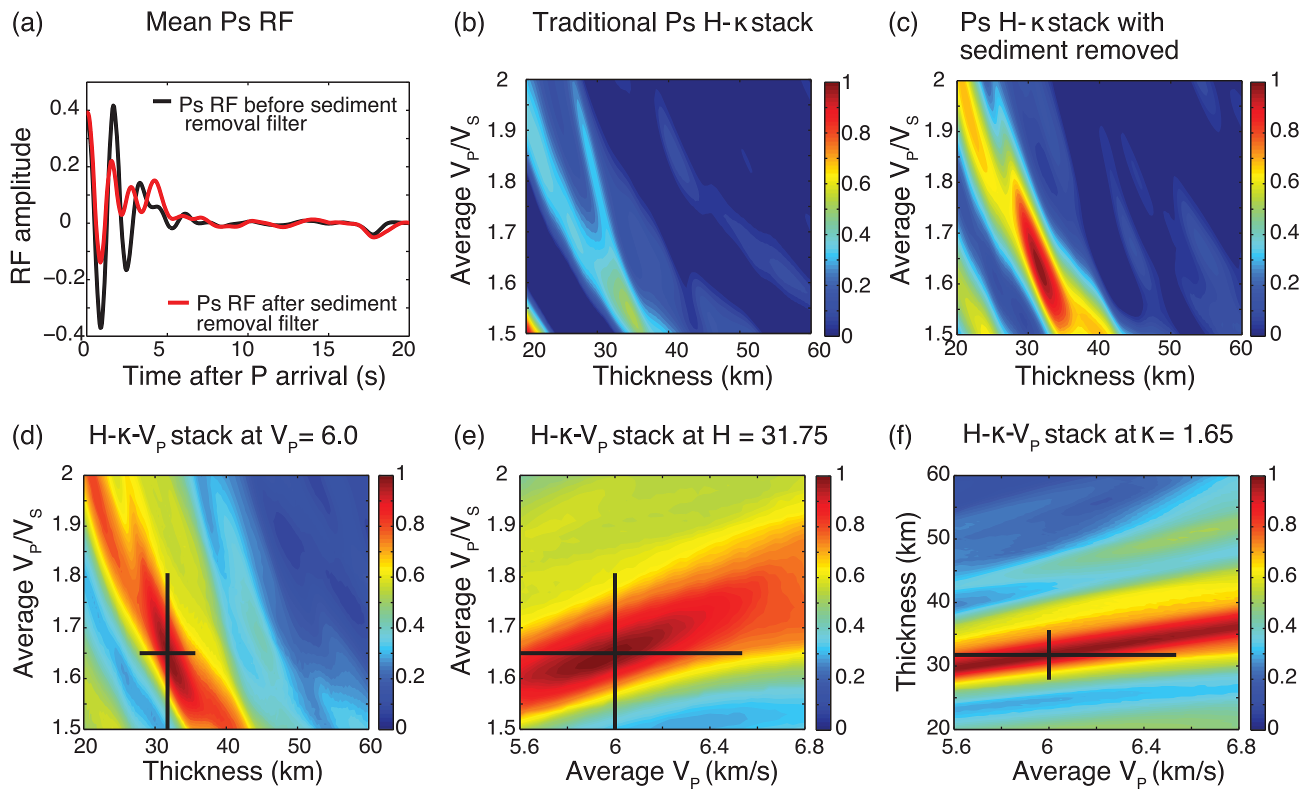

Figure 7. SRTC H–κ–V_P stacking of U60A receiver functions, where negative values in the stack are clipped. Station U60A is located on the Atlantic Coastal Plain in North Carolina. (a) The mean Ps receiver function before (black) and after (red) the sediment removal filter is applied. (b) Ps H–κ stack at assumed $V_P = 6.3\ \mathrm{km\,s^{-1}}$ shows no clear maxima. (c) The Ps H–κ stack after the sediment removal filter and time correction is applied has a clear maximum. (d, e and f) Three cross-sections through the maximum of the H–κ–V_P triple stack ; black cross-hairs denote 1σ error bars.

V_P (from Crust 2.0) of 6.53 km s^{-1} (Crotwell & Owens 2005). At this station, our crustal thickness estimate is closer to the EARS estimates at station US BRAL, with a lower V_P/V_S. The low V_P/V_S value found in this study is consistent with a more felsic crustal composition beneath this station (Christensen 1996).

5 DISCUSSION

By creating the SRTC H–κ–V_P stack, we address two of the major limitations of traditional H–κ stacking: contamination by sediment layers and the *a priori* assumption of an average crustal V_P.

In regions overlain by a sedimentary layer, such as the Williston basin, Atlantic coastal plain and Mississippi embayment, sediment reverberations overprint deeper crustal conversions and traditional H–κ stacking methods fail. Yeck *et al.* (2013) proposed the sequential H–κ stacking approach, which characterizes the sediment V_P/V_S and thickness, and uses the result to correct for sediment effects and interpret Moho depth. By using the resonance removal filter and time corrections of Yu *et al.* (2015), we are similarly able to characterize and suppress the S basin multiples, which are likely to dominate the reverberation signal (Fig. S7) before interpreting Moho depth. However, unlike sequential H–κ stacking, the SRTC H–κ stack is able to constrain crustal properties even when the S-basin multiple and Moho phase arrivals are coincident in time due to the sediment time corrections. Unlike Yu *et al.* (2015), we find that in practice, it is easier to use the arrival time of the PP_bs phase instead of the P_bs phase, due to its larger amplitude and larger lag-time.

Assuming an incorrect average crustal V_P may lead to biased estimates of the crustal thickness, even when no sedimentary layer is present (Yeck *et al.* 2013). The H–V stacking method of Rychert & Harmon (2016) uses the direct Sp arrival as well as Sp multiples (from the Sp RFs) to constrain average crustal V_P, V_S, and thickness, removing the dependence on average V_P. While this method is robust in areas without sedimentary reverberations, the low amplitude Sp multiples can make it difficult to use Sp RFs when substantial noise is present, which is often the case. For this reason, we choose to supplement the constraints provided by SRTC H–κ by incorporating only the direct Sp conversion in our stacks. The Sp phase arrival yields particularly useful constraints on the crustal thickness when the sediment structure has multiple layers (such as at station 448A) and/or when a clear P_ms is not observed even after the reverberation filter is applied. To constrain V_P, the SP_mp RF is also added, which has proven useful to constrain crustal thickness and velocity in a region where sediment is present (e.g. Parker *et al.* 2016).

A significant concern for the SP_mp phase is the effect of azimuthal anisotropy or dipping layers on the arrival time of the SP_mp phase. SP_mp is observed on a very restricted epicentral distance range (30–50°), and so to look at the variation in arrival time based on backazimuth (BAZ), binned SP_mp events are plotted over a range of BAZ bins for permeant seismic station ANMO used because it has events from a range of backazimuths. When plotted by BAZ, the SP_mp phase does not show a strong directional dependence for station ANMO (Fig. S9). This is especially significant as station ANMO lies near the Rio Grande Rift with the Colorado Plateau to the north and the basin and range to the south. The geological regions have differences in crustal properties and thickness that

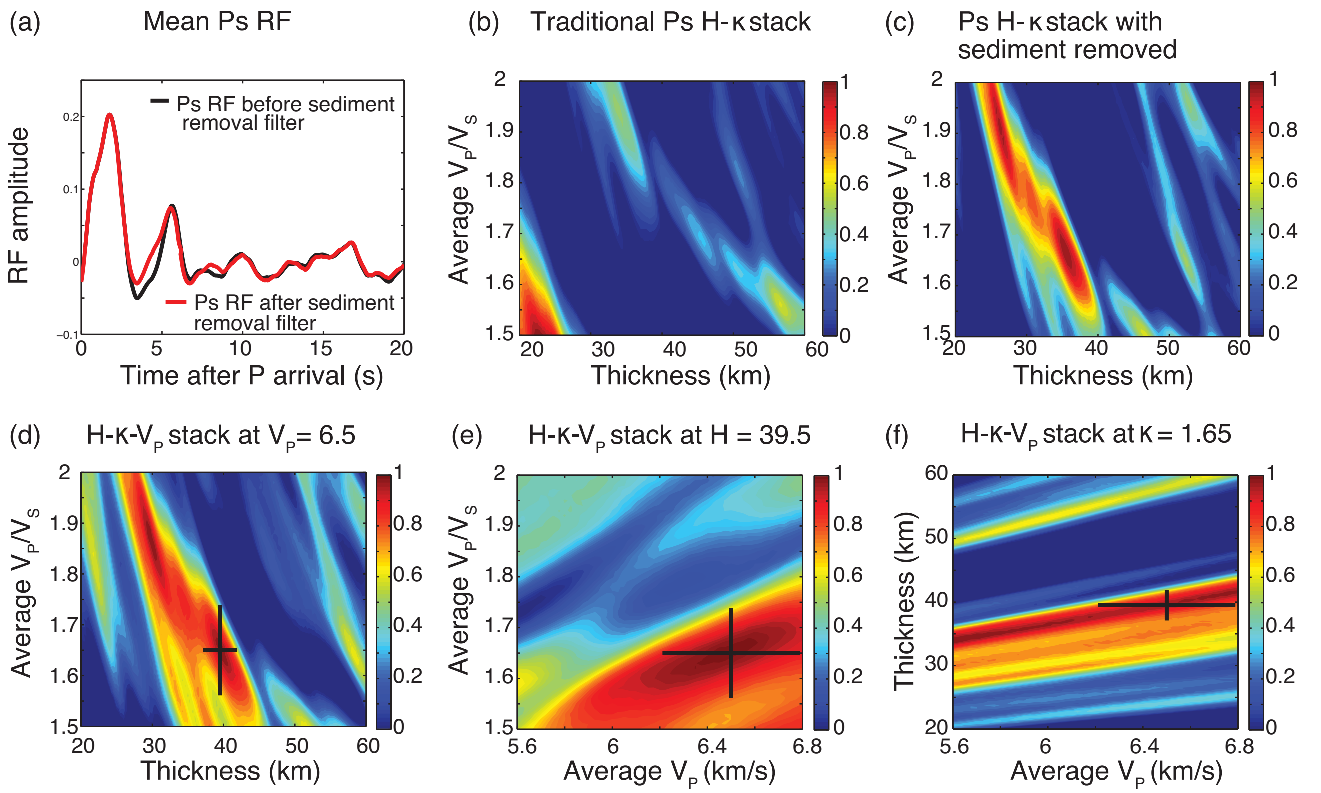

Figure 8. SRTC H–κ–V_P stacking of 448A receiver functions. Station 448A is located on the Mississippi Embayment in Mississippi. (a) The mean Ps receiver function before (grey) and after (red) the sediment removal filter is applied, which do not appear significantly different at this station. (b) Ps H–κ stack at assumed $V_P = 6.3$, and the maximum of the stack is $H = 24$ km and $\kappa = 1.5$. (c) The Ps H–κ stack after the sediment removal filter and time correction is applied has a maximum at $H = 36.25$ km and $\kappa = 1.83$. (d, e and f) Three cross-sections through the H–κ–V_P triple stack through the maximum of the stack; black cross-hairs denote 1σ error bars.

might be expected to manifest as backazimuthal variations in the SP_mp phase arrival; however, that is not the case, and the SP_mp phase shows a clear and consistent arrival from all BAZ bins with more than three existing events, suggesting that stacking SP_mp observed at a station is justified. Similar concerns exist for Sp and Ps phases in H–κ stacking, although the backazimuthal dependence of Sp due to anisotropy is expected to be very complex. In future studies, harmonic decomposition of Ps phases (e.g. Olugboji & Park 2016) can be used to detect and isolate the signature of anisotropy and/or dipping layers, helping to constrain average crustal anisotropy. Additionally, extra care must be taken when considering SP_mp RFs for stations near oceanic crust. Since the SP_mp waveform is affected by distant crustal structure, and oceanic and continental crust differ dramatically in thickness, analysis should be restricted to include only events with back azimuths that sample the continental crust.

The resonance removal filter will effectively remove S-wave reverberations associated with the low velocity layer in Ps RF. One concern is that contamination from additional sedimentary reverberations (such as PP_bs reverberations) may still mask the crustal phase arrivals even after the resonance removal filter is applied. We find that if the sedimentary V_S is very low (has an average velocity of less than 0.5 km s^{-1}) and sediment is thick (around 3 km), while the crust is very thin (less than 20 km) it is possible for large amplitude PP_bs to arrive at the same times as direct P_ms conversion from the Moho and its reverberations to arrive directly after Moho phases. In these rare cases, the sediment PP_bs phase may stack coherently near the maxima, biasing the crustal thickness estimate 0.5–1.0 km deeper than input values and V_P/V_S by 0.02–0.03 higher than input value and therefore, the SRTC H–κ–V_P triple stack may be contaminated by PP_bs and should not be used (Fig. S2 When the average sediment V_S is larger or the sediment is not as thick, S-wave reverberations are the dominant signal in the Ps receiver functions (Fig. 2, Fig. S1).

One limitation of the resonance removal filter is that it assumes a single shallow layer, and only removes reverberations from the largest amplitude resonances—typically, the S-wave reverberations—in the Ps RF. The way it has been implemented in this study, the resonance removal filter does not remove reverberations from multiple distinct shallow layers that may add further reverberations. While removing the largest reverberations is sufficient to constrain the crustal thickness and crustal average crustal velocities (V_P/V_S and V_P) at these stations, applying a secondary resonance removal filter could further reduce oscillatory conversions associated with multiple layers. For example, in the case of multiple low velocity sediment layers, a secondary resonance removal filter, applied after the first, may be able to remove reverberations associociated the layer bounded by second-largest impedance contrasts. In regions where S-wave reverberations of the whole crust are particularly prominent, an extension of this method may be to apply a secondary resonance removal filter to remove reverberations from the crust–mantle boundary (Moho) that can mask intra-lithospheric arrivals at approximately 7–10 s (about 80–100 km).

6 CONCLUSIONS

Traditional *H*–*κ* stacking is commonly used to constrain crustal thickness and V_P/V_S beneath a seismic station, but requires an assumed average crustal V_P and fails in the presence of a low velocity sedimentary layer. Previous studies have been able to remove sediment contamination (Yeck *et al.* 2013) or remove the dependence on average crustal V_P (Rychert & Harmond 2016) with some success. We present the sediment-removed, time corrected (SRTC) *H*–*κ*–V_P stacking method that is able to remove sediment contamination even when *S*-wave multiples directly overprint crustal signals while also yielding constraints on average crustal V_P.

The SRTC *H*–*κ*–V_P stacking method uses quantitative thresholds to determine whether large amplitude oscillatory sedimentary reverberations are present in the Ps RF. It then applies a resonance removal filter and time corrections from Yu *et al.* (2015) to the Ps RFs, and adds complementary Sp and SP_mp RFs, with their respective time corrections. Synthetic tests verify that this method is effective in constraining crustal properties when sediment reverberations contaminate deeper crustal conversions, even without removing *P*-wave multiples. When applied to EarthScope TA stations in the presence of sediment, our estimates of *H*, *κ* and V_P agree well with previous studies. At stations where traditional *H*–*κ* stacking implies an unlikely crustal thickness and V_P/V_S ratio, a more reasonable estimate for the crustal properties is obtained after the SRTC *H*–*κ*–V_P stacking method is applied. Because using the *H*–*κ*–V_P stacking method requires fewer *a priori* assumptions about the underlying crustal structure, including whether a sedimentary layer is present, it is straightforward to be applied to large seismic arrays regardless of geological/tectonic regime.

Both resonance removal and time corrections can reduce the complexity introduced into traditional *H*–*κ* stacks by shallow layer reverberations. We ensure that error calculations capture uncertainty arising from our ignorance about the values of the other parameters. This allows us to better define and estimate error around one clear maximum in the triple stack. However, this method does not provide an efficient way to express error if multiple maxima are present. For a large-scale study using the SRTC *H*–*κ*–V_P stacking, a complexity term based on the amplitude of the next closest maxima in the stack is suggested. In a regional study, when multiple maxima are present at a station, nearby stations can be used to constrain the correct crustal parameters in complex stacks, and a search range for *H*, *κ* and V_P be based on existing crustal models near the seismic station, such as Crust 2.0 (Crotwell & Owens 2005) can be implemented to constrain reasonable crustal values and reduce computation time.

Though our method avoids making prior assumptions about average crustal V_P, which is necessary in traditional *H*–*κ* stacking, V_P is often poorly constrained using this method, with error up to ± 0.6 km s^{-1}. While the constraint on crustal V_P is sufficient for this study, tighter constraints on crustal V_P may be necessary to for other applications, such as for drawing inferences about crustal composition. Even when including complementary Ps, Sp and SP_mp data, we find that the data are not particularly sensitive to V_P, which is reflected in our estimated errors (between 0.3 and 0.6 km s^{-1}). Where data from active source studies is available (e.g. Lithoprobe: Clowes *et al.* 1987; Cook *et al.* 1988; Hyndman *et al.* 1990; Lewry *et al.* 1994; Ross *et al.* 1995, or COCORP: Cook *et al.* 1979; Allemdinger *et al.* 1983; Petersen *et al.* 2010 seismic lines), they can provide tighter constraints on V_P than the triple-stacck method described here. Alternatively, joint inversion of receiver functions with surface wave data can better constrain crustal V_P (e.g. Julia *et al.* 2000a,; Lawerence & Wiens 2004a,; Shen *et al.* 2013a,b). Because our work suggests that removal of sediment multiples can clarify constraints from receiver functions, it is likely to improve results of such joint inversions.

From the Ps receiver functions and resonance removal filter, information is obtained that can be used to constrain sedimentary layers. Specifically, the amplitude and traveltime of the *S*-wave reverberation in the sediment that when combined with assumptions about the relationship of V_P and V_S may be used to estimate sedimentary thickness and velocity. Thick sedimentary layers lead to increased amplitude and duration ground shaking during a seismic event, so mapping the structure of sedimentary basins over large regions has implications for seismic hazard mapping.

ACKNOWLEDGEMENTS

The authors thank two anonymous reviewers for insightful and helpful comments that have improved this manuscript. The authors acknowledge support from the National Science Foundation (CAREEREAR-1352214) and from the Packard Foundation Fellowship to VL.

REFERENCES

Abt, D.L., Fischer, K.M., French, S.W., Ford, H.A., Yuan, H. & Romanowicz, B., 2010. North American lithospheric discontinuity structure imaged by Ps and Sp receiver functions, *J. geophys. Res.: Solid Earth,* **115,** 1–24.

Aki, , K. & Richards, , P.G., 1980. *Qunatitative Seismology,,* 2nd edition, University Science Books

Allmendinger, R.W., Sharp, J.W., Von Tish, D., Serpa, L., Brown, L., Kaufman, S., Oliver, J. & Smith, R.B., 1983. Cenozoic and Mesozoic structure of the eastern Basin and Range province, Utah, from COCORP seismic-reflection data, *Geology,* **11,** 532.

American Association of Petroleum Geologists. Basement Rock Project Committee and US Geological Survey, 1967. Basement map of North America between latitudes 24° and 60° N. US Geol. Survey.

Audet, P., Bostock, M.G., Christensen, N.I. & Peacock, S.M., 2009. Seismic evidence for overpressured subducted oceanic crust and megathrust fault sealing, *Nature,* **457,** 76–78.

Biryol, C.B., Lee, S.J., Lees, J.M. & Shore, M.J., 2018. Lithospheric structure of an incipient rift basin: results from receiver function analysis of Bransfield Strait, NW Antarctic Peninsula, *Polar Sci.,* 0–1, doi:10.1016/j.polar.2018.02.003.

Bostock, M.G., 1996. Ps conversions from the upper mantle transition zone beneath the Canadian landmass, *J. geophys. Res. Earth,* **101,** 8393–8402.

Bostock, M.G. & Kumar, M.R., 2010. Bias in seismic estimates of crustal properties, *Geophys. J. Int.,* **182,** 403–407.

Bracewell, R., 1968. *The Fourier Transform and Its Applications,* 2nd edn Integers. McGraw-Hill. doi:10.1119/1.1973431.

Brocher, T.M., 2005. Empirical relations between elastic wavespeeds and density in the Earth's crust, *Bull. seism. Soc. Am.,* **95,** 2081–2092.

Chai, C., Ammon, C.J., Maceira, M. & Herrmann, R.B., 2015. Inverting interpolated receiver functions with surface wave dispersion and gravity: application to the western U.S. and adjacent Canada and Mexico, *Geophys. Res. Lett.,* **42,** 4359–4366.

Christensen, , N.I., 1996. Poisson's ratio and crustal seismology, *J. geophys. Res,* **101,** 3139–3156.

Chulick, G.S. & Mooney, W.D., 2002. Seismic structure of the crust and uppermost mantle of north America and adjacent oceanic basins: a synthesis, *Bull. seism. Soc. Am.,* **92,** 2478–2492.

Clayton, R.W. & Wiggins, R.A., 1976. Source shape estimation and deconvolution of teleseismic body waves, *Geophys. J. R. astr. Soc.,* **47** (1), 151–177, .

Clowes, R.M., Brandon, M.T., Green, A.G., Yorath, C.J., Sutherland Brown, A., Kanasewich, E.R. & Spencer, C., 1987. LITHOPROBE-southern Vancouver Island: Cainozoic subduction complex image by deep seismic reflections, *Can. J. Earth Sci.,* **24,** 31–51.

Cook, F.A., Albaugh, D.S., Brown, L.D., Kaufmann, S., Oliver, J.E. & Hatcher, R.D., 1979. Thin-skinned tectonics in the crystalline southern Appalachians: COCORP seismic-reflection profiling of the Blue Ridge and Piedmont, *Geology,* **7**(12), 563–567.

Cook, F.A., Brown, L.D., Kaufman, S., Oliver, J.E. & Petersen, T.A., 1981. COCORP seismic profiling of the Appalachian orogen beneath the coastal plain of Georgia, *Bull. geol. Soc. Am.,* **92,** 738–748.

Cook, F.A. *et al.*, 1988. Lithoprobe seismic reflection structure of the Southeastern Canadian Cordillera: initial results, *Tectonics,* **7,** 157–180.

Crotwell, H.P. & Owens, T.J., 2005. Automated receiver function processing. *Seismol. Res. Lett.,* **76,** 702–709.

Dueker, K.G. & Sheehan, A.F., 1997. Mantle discontinuity structure from midpoint stacks of converted P to S waves across the Yellowstone hotspot track, *J. geophys. Res.: Solid Earth,* **102,** 8313–8327.

Eaton, D.W., Dineva, S. & Mereu, R., 2006. Crustal thickness and VP/VS variations in the Grenville orogen (Ontario, Canada) from analysis of teleseismic receiver functions, *Tectonophysics,* **420,** 223–238.

Farra, V. & Vinnik, L., 2000. Upper mantle stratification by P and S receiver functions, *Geophys. J. Int.,* **141**(3), 699–712.

French, S.W., Fischer, K.M., Syracuse, E.M. & Wysession, M.E., 2009. Crustal structure beneath the Florida-to-Edmonton broadband seismometer array, *Geophys. Res. Lett.,* **36,** L08309.

Hyndman, R.D., Yorath, C.J., Clowes, R.M. & Davis, E.E., 1990. The northern Cascadia subduction zone at Vancouver Island: seismic structure and tectonic history, *Can. J. Earth Sci.,* **27,** 313–329.

Julià, J., Ammon, C.J., Herrmann, R.B. & Correig, A.M., 2000. Joint inversion of receiver function and surface wave dispersion observations, *Geophys. J. Int.,* **143,** 99–112.

Kang, D., Yu, C., Ning, J. & Chen, W., 2016. Simultaneous determination of crustal thickness and P wavespeed by virtual deep seismic sounding (VDSS), *Seismol. Res. Lett.,* **87,** 1104–1111.

Kennett, B.L.N., 1991. The removal of free surface interactions from three-component seismograms, *Geophys. J. Int.,* **104,** 153–154.

Kikuchi, M. & Kanamori, H., 1982. Inversion of complex body waves, *Bull. seism. Soc. Am.,* **72,** 491–506.

Kumar, M.R. & Bostock, M.G., 2008. Extraction of absolute P velocity from receiver functions, *Geophys. J. Int.,* **175,** 515–519.

Kumar, M.R., Saul, J., Sarkar, D., Kind, R. & Shukla, A.K., 2001. Crustal structure of the Indian shield: new constraints from teleseismic receiver functions, *Geophys. Res. Lett.,* **28,** 1339–1342.

Langston, C.A., 1979. Structure under Mount Rainier, Washington, inferred from teleseismic body waves, *J. geophys. Res.,* **84,** 4749.

Langston, C.A., 1994. An integrated study of crustal structure and regional wave propagation for southeastern Missouri, *B. Seism. Soc. Am.,* **84,** 105–118.

Langston, C.A., 1996. The SsPmp phase in regional wave propagation, *Bull. seism. Soc. Am.,* **86,** 133–143.

Langston, C.A. & Horton, S.P., 2014. Three-dimensional seismic-velocity model for the unconsolidated mississippi embayment sediments from H/V ambient noise measurements, *Bull. seism. Soc. Am.,* **104,** 2349–2358.

Laske, G., Masters, G., Ma, Z. & Pasyanos, M., 2013. Update on CRUST1.0 -A 1-degree Global Model of Earth's Crust, *Geophys. Res. Abstr. EGU Gen. Assem.,* **15,** 2013–2658.

Lawrence, D.P. & Hoffman, C.W., 1993. Geology of Basement Rocks Beneath the North Carolina Coastal Plain.

Lawrence, J.F. & Shearer, P.M., 2006. Constraining seismic velocity and density for the mantle transition zone with reflected and transmitted waveforms, *Geochem., Geophys. Geosyst.,* **7,** doi:10.1029/2006GC001339.

Lawrence, J.F. & Wiens, D.A., 2004. Combined receiver-function and surface wave phase-velocity inversion using a niching genetic algorithm: application to Patagonia, *Bull. seism. Soc. Am.,* **94,** 977–987.

Leahy, G.M., Saltzer, R.L. & Schmedes, J., 2012. Imaging the shallow crust with teleseismic receiver functions, *Geophys. J. Int.,* **191,** 627–636.

Levander, A. & Miller, M.S., 2012. Evolutionary aspects of lithosphere discontinuity structure in the Western U.S., *Geochem., Geophys. Geosyst.,* **13,** doi:10.1029/2012GC004056.

Levin, V. & Park, J., 1997. *P-SH* conversions in a flat-layered medium with anisotropy of arbitrary orientation, *Geophys. J. Int.,* **131,** 253–266.

Lewry, J.F. *et al.*, 1994. Structure of a Paleoproterozoic continent-continent collision zone: a LITHOPROBE seismic reflection profile across the Trans-Hudson Orogen, Canada, *Tectonophysics,* **232,** 143–160.

Li, A., 2002. Crust and upper mantle discontinuity structure beneath eastern North America, *J. geophys. Res.,* **107,** 2100.

Ligorria, J.P. & Ammon, C.J., 1999. Iterative deconvolution and receiver-function estimation, *Bull. seism. Soc. Am.,* **89,** 1395–1400.

Lynner, C. & Porritt, R.W., 2017. Crustal structure across the eastern North American margin from ambient noise tomography, *Geophys. Res. Lett.,* **44,** 6651–6657.

Mooney, W.D., Andrews, M.C., Ginzburg, A., Peters, D.A. & Hamilton, R.M., 1983. Crustal structure of the northern Mississippi embayment and a comparison with other continental rift zones, *Dev. Geotecton.,* **19,** 327–348.

Musacchio, G., Mooney, W.D., Luetgert, J.H. & Christensen, N.I., 1997. Composition of the crust in the Grenville and Appalachian Provinces of North America inferred from V_P/V_S ratios, *J. geophys. Res.: Solid Earth,* **102,** 15225–15241.

Olugboji, T.M. & Park, J., 2016. Crustal anisotropy beneath Pacific Ocean-Islands from harmonic decomposition of receiver functions, *Geochem., Geophys. Geosyst.,* **17,** 810–832.

Owens, T.J. & Zandt, G., 1997. Implications of crustal property variations for models of Tibetan plateau evolution, *Nature,* **387,** 37–43.

Owens, T.J., Zandt, G. & Taylor, S.R., 1984. Seismic evidence for an ancient rift beneath the Cumberland Plateau, Tennessee: a detailed analysis of broadband teleseismic P waveforms, *J. geophys. Res.,* **89,** 7783–7795.

Parker, E.H., Hawman, R.B., Fischer, K.M. & Wagner, L.S., 2013. Crustal evolution across the southern Appalachians: initial results from the SESAME broadband array, *Geophys. Res. Lett.,* **40,** 3853–3857.

Parker, E.H., Hawman, R.B., Fischer, K.M. & Wagner, L.S., 2016. Estimating crustal thickness using SsPmp in regions covered by low-velocity sediments: imaging the Moho beneath the Southeastern Suture of the Appalachian Margin Experiment (SESAME) array, SE Atlantic Coastal Plain, *Geophys. Res. Lett.,* **43,** 9627–9635.

Pesce, K.A., 2010. *Comparison of Receiver Function Deconvolution Techniques*. Massachusetts Insitute of Technology.

Petersen, T.A., Brown, L.D., Cook, F.A., Kaufman, S. & Jack, E., 2010. Structure of the Riddleville Basin from COCORP seismic data and implications for reactivation tectonics Published by : The University of Chicago Press Stable URL :http://www.jstor.org/stable/30069399, *Geology,* **92,** 261–271.

Ramesh, D.S., Kind, R. & Yuan, X., 2002. Receiver function analysis of the North American crust and upper mantle, *Geophys. J. Int.,* **150,** 91–108.

Reeves, Z., Lekić, V., Schmerr, N., Kohler, M. & Weeraratne, D., 2015. Lithospheric structure across the California Continental Borderland from receiver functions, *Geochem., Geophys. Geosyst.,* **16,** 246–266.

Ross, G.M., Milkereit, B., Eaton, D., White, D., Kanasewich, E.R. & Burianyk, M.J.A., 1995. Paleoproterozoic collisional orogen beneath the Western Canada Sedimentary Basin imaged by Lithoprobe crustal seismic-reflection data, *Geology,* **23,** 195–199.

Rychert, C.A. & Harmon, N., 2016. Stacked P-to-S and S-to-P receiver functions determination of crustal thickness, Vp, and Vs: the H-V stacking method, *Geophys. Res. Lett.,* **43,** 1487–1494.

Rychert, C.A., Rondenay, S. & Fischer, K.M., 2007. P-to-S and S-to-P imaging of a sharp lithosphere-asthenosphere boundary beneath eastern North America, *J. geophys. Res.: Solid Earth,* **112,** 1–21.

Schimmel,, M. & ,Paulssen, H., 1997. Noise reduction and dectection of weak,coherant signals through phase-weighted stacks , *Geophys J Int,* **130 ,** 497–505.

Schulte-Pelkum, V., Mahan, K.H., Shen, W. & Stachnik, J.C., 2017. The distribution and composition of high-velocity lower crust across the continental U.S.: comparison of seismic and xenolith data and implications for lithospheric dynamics and history, *Tectonics,* **36,** 1455–1496.

Sheehan, A.F., Abers, G.A., Jones, C.H. & Lerner-Lam, A.L., 1995. Crustal thickness variations across the Colorado Rocky Mountains from teleseismic receiver functions, *J. geophys. Res.,* **100,** 20391.

Shen, W., Ritzwoller, M.H. & Schulte-Pelkum, V., 2013a. A 3-D model of the crust and uppermost mantle beneath the Central and Western US

by joint inversion of receiver functions and surface wave dispersion, *J. geophys. Res.: Solid Earth,* **118,** 262–276.
Shen, W., Ritzwoller, M.H. & Schulte-Pelkum, V., 2013b. A 3-D model of the crust and uppermost mantle beneath the Central and Western US by joint inversion of receiver functions and surface wave dispersion, *J. geophys. Res.: Solid Earth,* **118,** 262–276.
Sivia, D., 2006. *Data Analysis:A Bayesian Tutorial,* 2nd edn, Oxford University Press.
SotocCordero, L., Meltzer, A. & Stachnik, J.C., 2018. Crustal structure, intraplate seismicity, and seismic hazard in the mid-Atlantic United States, *Seismol. Res. Lett.,* **89,** 241–252.
Tian, X. *et al.*, 2015. Weakly coupled lithospheric extension in southern Tibet, *Earth planet. Sci. Lett.,* **430,** 171–177.
Vinnik, L.P., 1977. Detection of waves converted from P to SV in the mantle, *Phys. Earth planet. Inter.,* **15,** 39–45.
Warren, D.H., Healy, J.H. & Jackson, W.H., 1966. Crustal seismic measurements in southern Mississippi, *J. geophys. Res.,* **71,** 3437–3458.
C.Wilson,, D. , A.Angus,, D., ,Ni, J.F. & , .Grand, S.P, 2006, Constraints on the interpretation of S-to-P receiver functions *Geophys J Int ,* **165,** 969–980
Wölbern, I. & Rümpker, G., 2017. Limitations of H-κ stacking: ambiguous results caused by crustal layering, *J. Seismol.,* **21,** 221–235.
Yeck, W.L., Sheehan, A.F. & Schulte-Pelkum, V., 2013. Sequential H-κ stacking to obtain accurate crustal thicknesses beneath sedimentary basins, *Bull. seism. Soc. Am.,* **103,** 2142–2150.
Yuan, H., Dueker, K. & Stachnik, J., 2010. Crustal structure and thickness along the Yellowstone hot spot track: evidence for lower crustal outflow from beneath the eastern Snake River Plain, *Geochem., Geophys. Geosyst.,* **11,** 1–14.
Yu, C.Q., Chen, W.P., Ning, J.Y., Tao, K., Tseng, T.L., Fang, X.D., John Chen, Y. & van der Hilst, R.D., 2012. Thick crust beneath the Ordos plateau: implications for instability of the North China craton, *Earth planet. Sci. Lett.,* **357–358,** 366–375.
Yu, Y., Song, J., Liu, K.H. & Gao, S.S., 2015. Determining crustal structure beneath seismic stations overlying a low-velocity sedimentary layer using receiver functions, *J. geophys. Res.: Solid Earth,* **120,** 3208–3218.
Zelt, B.C. & Ellis, R.M., 1999. Receiver-function studies in the Trans-Hudson Orogen, Saskatchewan, *Can. J. Earth Sci.,* **603,** 585–603.
Zhu, L. & Kanamori, H., 2000. Moho depth variation in southern California from teleseismic receiver functions, *J. geophys. Res.,* **105,** 2969–2980.

SUPPORTING INFORMATION

Supplementary data are available at *GJI* online.

Table S1. Number of events and slowness range at each station.
Figure S1. Absolute value of the reflection coefficients of PP∗PP (left) and SS∗SS (right) for a range of different sediment velocity variables using equations from Aki & Richards (1980). Because the amplitude of each reverberation gets multiplied by these reflection coefficients, *P*-wave reverberations get smaller faster than the *S*-wave reverberations. This is why only *S*-wave reverberations remain visible in the Ps receiver functions analysed here (e.g. see Fig. 2).
Figure S2. The SRTC *H*–κ–V_P stacking method may not work when the PP_bs and P_ms phases arrival at the same time. Left-hand panel: calculated PP_bs arrival times as a function of sediment thickness and V_S. To ensure realistic behaviour, the V_P/V_S ratio changes according to the mud-line equation (Brocher 2005). Right-hand panel: the P_ms –PP_bs arrival time for a crust with $V_P = 6$ km s^{-1} and $V_P/V_S = 1.76$. Conditions under which the PP_bs arrival may interfere with the P_ms Moho arrival are shown in light blue to red. SRTC stacking may not work for an extremely thin crust of 20 km, if sediment thickness is greater than 1.5 km with an excessively low V_S of 0.5 km s^{-1}. We note that this is a highly unlikely set of conditions.
Figure S3. Dependence of resonance removal filter on ray parameter for an idealized synthetic case. The best-fitting reverberation removal filter (red line) calculated from the autocorrelation of the mean synthetic receiver function provides a good fit to the autocorrelations of Ps RFs computed across the range of possible ray parameters (black lines). The synthetic model used has a sediment layer 0.5 km thick with a $V_P = 2.5$ km s^{-1} and a $V_S = 1.7$ km s^{-1} overlying a 39.5 km crust with $V_P = 6.2$ km s^{-1} and $V_S = 3.5$ km s^{-1} and mantle with $V_P = 8$ km s^{-1} and $V_S = 4.5$ km s^{-1}.
Figure S4. *H*–κ–V_P stacks generated from synthetic waveforms with increasing noise levels. The input model has a sedimentary layer 0.5 km thick, V_P of 2.3 km s^{-1} and $\kappa = 2.3$, a Moho at 42.5 km depth with crustal $V_P = 6.3$ km s^{-1}, and a κ of 1.76. White noise is filtered to have similar frequency content as typically encountered noise, with amplitude up to three-quarters of the maximum of the daughter waveform (s for Ps; p for Sp and SP_mp). At increased noise levels, we are still able to constrain crustal *H*, κ and V_P: Mean 4 Hz (blue) and 1 Hz (black) Ps RF for station B30A. Red and magenta dots denote picked arrival times for δtP and δt, respectively. The arrival times of the two phases (P_bs and PP_bs) are indistinguishable at this station. (Bottom) Autocorrelation from the mean 4 Hz (blue) and 1 Hz (black) RF with picked arrival time for Δ*t*. Autocorrelation of a random subset of individual RFs are shown as grey lines in the background. At station B30A, the arrival time of Δ*t* does not depend on event location or frequency of autocorrelated RFs.
Figure S6. Top panel: Mean 4 Hz (blue) and 1 Hz (black) Ps RF for station U60A. Red and magenta dots denote picked arrival times for δtP and δt, respectively. The arrival time of the two phases (P_bs and PP_bs) are indistinguishable at this station. Bottom panel: autocorrelation from the mean 4 Hz (blue) and 1 Hz (black) RF with picked arrival time for Δ*t*. Autocorrelation of a random subset of individual RFs are shown as grey lines in the background. At station B30A, the arrival time of Δ*t* does not depend on event location and only changes slightly with frequency of autocorrelated RFs.
Figure S7. Top panel: mean 4 Hz (blue) and 1 Hz (black) Ps RF for station 448A. Red and magenta dots denote picked arrival times for δtP and δt, respectively. The arrival time of the two phases (P_bs and PP_bs) are substantially different station. Bottom panel: autocorrelation from the mean 4 Hz (blue) and 1 Hz (black) RF with picked arrival time for Δ*t*. Autocorrelation of a random subset of individual RFs are shown as grey lines in the background. At station 448A, the arrival time of Δ*t* is challenging to pick, possibly due to remaining reverberations from P-multiples, but more likely due to the multiple sediment layers (multiple negative bumps seen in the 4 Hz autocorrelation).
Figure S8. 1 Hz Ps receiver functions before (black) and after (red) sediment removal filter is applied plotted from 0 to 20 s after the direct *P* arrival. Top panel: station B30A, middle panel: station U60A and bottom panel: station 448A.
Figure S9. SP_mp RFs for events between 30 and 50 epicentral distances. Each line is a bin of backazimuthal (BAZ) directions from station ANMO, chosen due to its large range in BAZ of SP_mp events. The amplitude and location of the SP_mp at ∼6 s does not change significantly based on BAZ direction which indicates that the SP_mp waveforms show evidence of neither crustal anisotropy nor crustal thickness variations with BAZ. We expect this observation to hold true for most other stations, due to the low frequency of SP_mp waveforms.

Please note: Oxford University Press is not responsible for the content or functionality of any supporting materials supplied by the authors. Any queries (other than missing material) should be directed to the corresponding author for the paper.